Light induced charge transfer processes and pyroelectric luminescence in $Sn_2P_2S_6$

By

Andreas Rüdiger

submitted in partial fulfillment of the
requirements for the degree of
doctor rerum naturalium
at
university of osnabrück
osnabrück, germany
july 2001

Contents

Chapter 1

Introduction

The best known inorganic photorefractive crystals are oxides, such as $LiNbO_3$, $BaTiO_3$, $KNbO_3$ and related compounds. In comparison to them, ferroelectric $Sn_2P_2S_6$, investigated in this work, looks rather exotic. Its properties, including the band gap of about 2.3 eV, are closer to those of photorefractive semiconductors such as GaAs and CdTe. Like these materials, tending to have a higher photorefractive sensitivity in the infrared, $Sn_2P_2S_6$ is of interest because of its fast response, e.g. at 1060 nm. This allows to use the material in conjunction with Nd-YAG-lasers. The second harmonic of the 1064 nm emission fits to the bandgap of $Sn_2P_2S_6$, and recently fast holography by band-band transitions has been realized in this way [1].

The knowledge about the structure of defects, including its chemical, geometric, electronic and energetic characteristics, is decisive to tailor the photorefractive properties of a material. In contrast to the situation for simple semiconductors, for which the investigation of lattice perturbations has a long history, almost nothing is known in this respect for $Sn_2P_2S_6$. As a second distinguishing feature, $Sn_2P_2S_6$ can be sensitized for its infrared response by preillumination across the bandgap. Compared to the initial state, this can increase the photorefractive gain by a factor of about six [2]. The excited crystal state obtained in that way is metastable, not decaying for weeks if kept below the ferroelectric phase transition of the material, $T_C \approx 340\ K$. The situation thus defines two fields of investigation: Studies of the defect scenario in $Sn_2P_2S_6$, comprising the light induced charge transfer processes, and identification of the origin of the tremendous metastability.

These two fields are addressed in this thesis. Based on previous experience with studies of defects in oxide materials, electron paramagnetic resonance (EPR) methods, combined with simultaneous investigation of optical absorption changes, are utilized to unravel the defect scene of $Sn_2P_2S_6$. It turns out that the metastability of the material in its preilluminated state, is intrinsically connected with its feature of thermally stimulated luminescence. In pyroelectric

materials, such as $Sn_2P_2S_6$, this feature is superimposed to a special variant, called 'pyroelectric luminescence'. A model is proposed which is able to explain the essential features of this phenomenon. It appears that these studies are paradigmatic for the whole class of pyroelectrics.

The thesis is organized as follows: After this introduction, the global macroscopic and microscopic properties of $Sn_2P_2S_6$ are briefly summarized. The methods employed in this investigation are then described. Experimental results of the light-induced charge transfer are presented and discussed in the following chapters. A separate section is devoted to the phenomenon of pyroelectric luminescence and its explanation. The summary is followed by three appendices where special aspects are treated in an extended manner.

Chapter 2

Material

The promising holographic properties of $Sn_2P_2S_6$ especially in the near infrared have often been discussed [3, 4, 5, 6, 2, 7, 1, 8, 9]. Effective photorefractivity requires the interaction of several material properties, including those of the host lattice as well as of defects [10] [1]. The notation of $Sn_2P_2S_6$ already reveals more than only the composition. *Di-tin hexathiohypodiphosphate* indicates the composition and stoichiometry and *hypo* stresses that phosphorus occurs in a lower oxidation state than usually expected. For phosphorus usually either P^{3+} or P^{5+} is known, nevertheless the formula and the common oxidation states (Sn:2+ and S:2-) predict P^{4+}.

$$(Sn_2^{2+})^{4+} \quad (P_2^{4+})^{8+} \quad (S_6^{2-})^{12-} \tag{2.1}$$

However, P^{4+} is chemically unstable. There are two different ways to describe the situation more appropriately:

$$(Sn_2^{2+})^{4+} \quad (P_2^{3+/5+})^{4+} \quad (S_6^{2-})^{12-} \tag{2.2}$$

or, hiding the internal structure of the anion and in any respect less suggestive:

$$(Sn_2^{2+})^{4+} \quad (P_2S_6)^{4-} \tag{2.3}$$

Electron density calculations [11] and XPS measurements [12] confirm the existence of the Sn^{2+} ions. The $P_2S_6^{4-}$ unit remains completely unchanged during the ferroelectric phase transition. It is often referred to as an ethane-like structure because of its bipyramidal shape reminding of the C_2H_6-molecule.

2.1 Crystal structure

Confusion often arose from the different possible choices of the unit cell used in the literature. We shall point out the main structural elements in the low

[1] For all readers familiar with Russian or Ukrainian: D.M. Bercha, Yu.V. Voroshilov, V.Yu. Slivka, I.D. Turyanitsa, "Slozhnye khalkogenidy i khalkogengalodenidy", Lvov, LGU, published in 1983, may be an interesting review of the ferroelectric properties of $Sn_2P_2S_6$

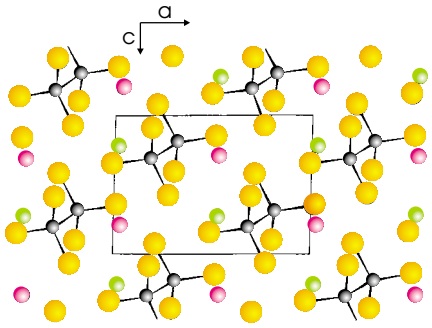

Figure 2.1: *The structure of $Sn_2P_2S_6$ as seen along [0 1 0] onto the a,c plane. Orange spheres indicate the position of sulfur, black one phosphorus, green and pink ones the position of Sn_{f1} and Sn_{f2}.*

symmetry of $Sn_2P_2S_6$. The main components are two tin cations and a (P_2S_6)-unit.

2.1.1 Space group

The space group describes which symmetry operations are allowed in a crystal. $Sn_2P_2S_6$ has a comparatively low symmetry in its monoclinic space group. Monoclinic here implies $a \neq b \neq c$ and $\alpha = \gamma = 90^o, \beta \neq 90^o$.

	a	b	c	α	β	γ	reference
rhombohedral	5.98	(5.98)	19.32	90	90	120	[13]
monoclinic I	5.99	10.36	6.80	90	107.1	90	[13]
monoclinic II	6.529[a]	7.485	11.317	90	124.1	90	[14]
monoclinic II	9.378	7.488	6.513[a]	90	91.15	90	[15]

[a] Although both groups claim an experimental precision of three digits, it is evident that the experimental error is larger. As shown in figure 2.2 these two values describe the same distance. The experimental accuracy is therefore assumed to be three digits only.

Table 2.1: *The crystal systems of $Sn_2P_2S_6$ and the two common space group notations for monoclinic II. All samples investigated in this thesis are considered to belong to this crystal system.*

The monoclinic II phase has three different notations, two of which are commonly referred to. Ambiguity arises from the low symmetry that allows the choice of different equivalent unit cells. The only feature that is fixed in the space group P_C is a glide plane and a vector (usually $\vec{b}$) perpendicular to that plane. Conventionally $\vec{a}, \vec{b}$ and $\vec{c}$ are a right handed system. The spontaneous polarization has to be in the glide plane. As can be seen from table 2.1 the notation chosen from Dittmar and Schäfer [15] offers a major advantage. This system is pseudo-orthorhombic. Many considerations become more comfortable as soon as we make use of the near orthorhombicity.

Figure 2.2 gives a view onto the (1 0 1)-plane along a [0 -1 0] direction (i.e. $\vec{b}$ is pointing towards you). Both unit cells include twice the volume of the primitive

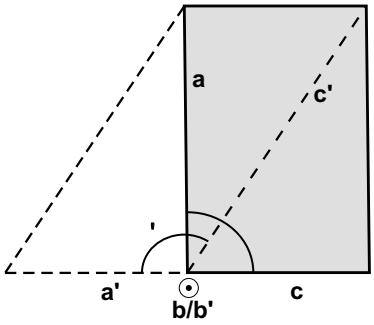

Figure 2.2: *The gray slightly distorted rectangle is the unit cell P_n according to Dittmar and Schäfer [15] true to scale. It is represented by a, b, c and β. The system P_{1c1} chosen by Carpentier and Nitsche [14] is denoted by a', b', c' and β'. The exact dimensions are given in table 2.1.*

elementary cell. As long as it is not explicitly mentioned to be different, all further considerations refer to the P_n notation chosen by Dittmar and Schäfer [15].

2.1.2 Domains

$Sn_2P_2S_6$ has ferroelectric 180°-domains. These domains are optically identical and cannot be visualized by crossed polarizers. Their investigation requires methods such as "gain topography" [16]. The existence of domains drastically reduces the two-beam-coupling efficiency. To avoid them, the samples need to be poled. Such poling is critical not only because of the fragility of the sample. Application of electrodes and especially their removal easily damages the sample. Special care was taken during the poling treatment. Poling for holographic purpose was done in a silicon oil bath in Kiev. Alternatively, poling in nitrogen atmosphere was used in Osnabrueck. In any case the presence of oxygen has to be avoided under heating. Since oxygen is not present in the lattice the partial pressure of atmospheric oxygen enables diffusion into the crystal.

2.2 Samples

The samples presented in this thesis are grown by A. Grabar from the Institute of Physics and Chemistry of Uzhgorod State University in Ukraine by vapor transport. They are of good optical quality. Unless explicitly mentioned, they are not poled. After some experiments and handling the edges of $Sn_2P_2S_6$ are often cracked.

2.2.1 Nominally pure $Sn_2P_2S_6$

In general "nominally pure" in this context means that no dopants were intentionally added. It cannot be excluded that background contaminations occur. These contaminations in the order of a few parts per million (ppm) can be sufficient, e.g. in $LiNbO_3$:Fe, to induce photorefractivity.

name	dimension (mm × mm × mm)	comment
K3	3,4,1	fragment, nominally pure, type I
K2	8,2,2	nominally pure, type II
N4	5,4,4	nominally pure
SPS 12	7,3,3	nominally pure
New1	4,3,3	nominally pure
SPS:Se	3,3,1	0.5 wt% Se
SPS:Fe	3,3,2	0.5 wt% Fe, fragments
old dark	3,2,1	fragments
new dark	5,4,3	nominally pure

Table 2.2: List of available samples and their dimensions.

A subdivision between nominally pure $Sn_2P_2S_6$ crystals became necessary when Shumelyuk [7] performed holographic experiments with different nominally undoped samples and obtained results that were not only depending on the treatment but also on the samples themselves. In some specimens pre-exposure to "white light" of a halogen bulb increases the holographic gain by a factor of 6 as reported by Odoulov et al. [2] whereas in other samples the same procedure has no effect on the holographic gain. Nothing is known about the mechanism and the defect structure that enables such desirable features.

Type I

The nominally pure crystal K3 with excellent holographic performance shows the feature of light-induced sensitization. Most parameters of the light-induced charge transfer for infrared holographic recording are determined with this particular sample. This light-induced sensitization lasts for at least several days up to several weeks.

Type II

Sample K2, though grown in the same way as K3, shows no light induced sensitization. This allows three interpretations: 1) the light induced sensitization is a general property of all $Sn_2P_2S_6$ crystals but is suppressed by certain defects in type II samples 2) the light induced sensitivity is induced by special defects only present in type I crystals 3) the light induced sensitization is induced by special defects in type I and impeded by other defects in type II samples. Type I and type II samples differ in their holographic spectral response [7] as well. This difference could be explained by different effective trap densities.
Among the crystals investigated in the framework of [7], the ratio of samples corresponding either to type I or type II behaved roughly as 1:1. There is no evident preference to the one or the other state. In any of the above explanations defects are involved and the fact, that at least about 50% of all samples have unintended dopants shows that the samples are far from being "pure".

2.2.2 Doped $Sn_2P_2S_6$

$Sn_2P_2S_6$ has also been grown with various dopants, e.g. Fe, Mn, Se, Pb. Unless there is detailed knowledge of the incorporation of the defect ions it is difficult to estimate the effect of dopants. The vapor transport growth has the drawback that the transport gas itself cannot be excluded as contamination and that silicon from the quartz tubes may be incorporated into the bulk. Moreover simple exposure to air containing oxygen will probably cause diffusion of oxygen onto the isoelectronic sulfur site, especially if we take into account the sulfur deficiency (see section A.3).

$Sn_2P_2S_6$:Fe (0.5 % wt)

Iron is one of the most favorable dopants for photorefractive purposes in other materials such as $LiNbO_3$ and $BaTiO_3$. It can occur in different valence states (Fe^{2+}, Fe^{3+}, Fe^{4+} and Fe^{5+}) and is active in a concentration of a few ppm. In $Sn_2P_2S_6$ it has been intentionally added in an amount of 0.5% wt. However, the solubility of Fe in the crystal may be low, and the defect concentration may thus be much lower. Since the compound $Fe_2P_2S_6$ can be prepared, it is expected that Fe is incorporated at Sn sites.

$Sn_2P_2S_6$:Se (0.5 % wt)

Selenium is isoelectronic to sulfur and will be favorably incorporated at sulfur sites inducing a distortion of the (P_2S_6)-unit, since it is larger than sulfur. The integration of selenium increases the polarity of the material [17] and in larger concentration it decreases the phase transition temperature. An additional effect is observed for a selenium amount exceeding 29%, where an incommensurate phase occurs [18]. This phase is, roughly spoken, a coexistence of para- and ferroelectric phase.
As a defect, selenium is known to have a high affinity for trapping holes.

Dark $Sn_2P_2S_6$

The so called 'dark' or 'brown' $Sn_2P_2S_6$ is grown with SnI_2 as transport gas instead of SnI_4. Absorption spectra exhibit an additional rather pronounced band close to the fundamental absorption. Moreover the holographic performance is enormous: no photo-sensitization is necessary to enhance the holographic gain, which can be as large as $\Gamma = 12\text{cm}^{-1}$. That means that a defect is present that works the same way as the defect that is created by illumination with white light. The very first dark $Sn_2P_2S_6$ was grown under conditions that could not be reproduced for a long time [19].

2.3 Macroscopic properties

The lack of a center of inversion is a necessary precondition for some macroscopic features such as a linear electrooptic effect, pyroelectricity and piezoelectricity.

The latter two result from different centers of mass for negative and positive lattice components. Pyroelectricity is always accompanied by piezoelectricity, not necessarily vice versa.

2.3.1 Ferroelectricity

In the paraelectric phase both tin sites Sn_p^{2+} are equivalent in any respect. In the ferroelectric phase the two Sn^{2+} ions subsequently denoted as Sn_{f1}^{2+} and Sn_{f2}^{2+} [2] move differently. Sn_{f1}^{2+} shifts 0.032 nm along [1 0 0] and 0.004 nm along [0 0 1] whereas Sn_{f2}^{2+} moves 0.023 nm along [1 0 0], 0.003 nm along [0 0 1] and 0.004 nm along [0 1 0][20, 21].
Since we will refer to this later (see chapter 5), it is worth mentioning, that in the ferroelectric phase one Sn is coordinated by 7 S ions while the other is coordinated by 8 S ions.
For a detailed reference to positions, angles, distances and coordination see [15].

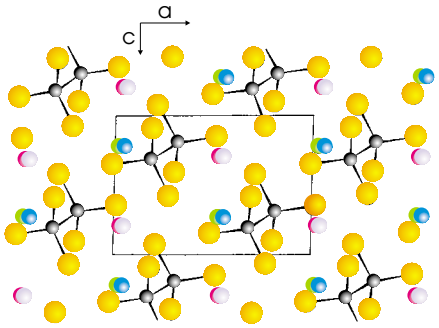

Figure 2.3: *The displacement of Sn_{f1}^{2+} and Sn_{f2}^{2+} according [20, 21] true to scale. The red and green spheres in the background indicating the previous positions are exchanged by violet and blue.*

The volume of the unit cell is $457.27 \cdot 10^{-30} m^3$ [15] containing twice the volume of the primitive unit cell. We are now able to give an estimation of the spontaneous polarization by division of the electric dipole momentum of the unit cell by its volume. The displacement of the positive center of mass with respect to the negative is about 0.027 nm. Since four elementary charges are displaced and two units are involved in our cell, we obtain:

$$p = 4 \cdot 2 \cdot ed \tag{2.4}$$

$$P = \frac{p}{V} = 7.57 \cdot 10^{-2}\ C\,m^{-2} \tag{2.5}$$

The other lattice subunit is the "ethan-like" $(P_2S_6)^{4-}$ anion. This unit is characterized by a phosphorus pair, covalently bound, and 3 sulfur atoms attached to each phosphorus. The exact binding lengths are published in [15]. This subunit is hardly changed during the phase transition. Only a faint shift of the polyhedra of sulfur is observed.

[2] f (ferroelectric), p will denote paraelectric

The spontaneous polarization is a first rank tensor (i.e. a polar vector) with up to 3 independent components that can be written in different ways depending on the choice of the unit cell (see section 2.1.1). In the notation of Dittmar and Schäfer [15] the polarization is along [1 0 0]. Symmetry considerations only require that the spontaneous polarization lies in the symmetry-plane, i.e. $\vec{b}$ is perpendicular to the the spontaneous polarization:

$$\vec{P}_s = \begin{pmatrix} 1.4 \cdot 10^{-1} C m^{-2} \\ 0 \\ 0 \end{pmatrix} \tag{2.6}$$

This value was first measured by Carpentier and Nitsche [20] and is typical of photorefractives such as $LiNbO_3$. Note that it is of the order of magnitude as expected from the dipole moment of the unit cell (cf. Eq. 2.5).
The coercive field is about 750 V/cm at room temperature though it significantly varies with the polarization state of the samples. The spontaneous polarization is a sensitive tool for the determination of phase transitions, and was employed by Buturlakin et al. [22] to elaborate the phenomenology of the ferroelectric phase transition.

Pyroelectricity

Since $Sn_2P_2S_6$ is ferroelectric with a displacive phase transition close to room temperature, it is not surprising that pyroelectricity occurs. Bravina et al. [23] report a pyroelectric coefficient γ ranging between $0.9\,C\,m^{-2}\,K^{-1}$ and $7\,C\,m^{-2}\,K^{-1}$ at 295 K. The higher the absolute value of the pyroelectric coefficient, the better was the polarization state.
The temperature dependence of γ is difficult to determine, since the conductivity and the thermal elongation have to be taken into account. The latter contributes via stiffness and piezoelectric tensor to the pyroelectric coefficient. Maior et al. [24] published a value of $\gamma = 0.9\,C\,m^{-2}\,K^{-1}$. As an approximation we can use the thermodynamic relation between the pyroelectric coefficient and ϵ to determine $\gamma(T)$:

$$P = (\epsilon - 1)\epsilon_0 E \tag{2.7}$$

$$\frac{dP}{dT} = \frac{d}{dT}(\epsilon - 1)\epsilon_0 E \tag{2.8}$$

$$\gamma = \frac{d\epsilon}{dT}(\epsilon_0 E) \tag{2.9}$$

As mentioned, there is a substantial difference in the origin of the pyroelectric field depending on whether the sample is *free* (primary and secondary pyroelectric effect) or *clamped* (primary pyroelectric effect) [3]. A free sample will elongate or contract due to thermal deformation (f_{ij} as the tensor of deformation)

[3] This is analogous to the electrooptic effect

$$f_{ij} = \kappa_{ij}\Delta T \tag{2.10}$$

This results in internal stresses that will have a contribution to the overall electric field arising from piezoelectricity. The general correspondence between the primary pyroelectric coefficient γ_i^{p} and the secondary pyroelectric coefficient γ_i^{s} is given by [25]:

$$\gamma_i = \gamma_i^{\mathrm{p}} + \pi_{ijk}\xi_{jklm}\kappa_{lm} \tag{2.11}$$

with $i, j, k... = 1, 2, 3$. The secondary pyroelectric coefficient is given by the product of π_{ijk} which denotes the third rank piezoelectric tensor, ξ_{jklm} being the fourth rank stiffness tensor and κ_{lm}, the second rank tensor of thermal expansion. These tensors are not completely known and cannot be experimentally separated, so a complete separation of primary and secondary pyroelectric effect is impossible.

Piezoelectricity

All ferroelectrics show a considerable piezo-effect described by a third rank tensor that feeds back to other properties such as the difference of free and clamped elements of the electrooptic and pyroelectric tensor. The tensor elements are difficult to obtain since due to the low hardness and good fissility of $Sn_2P_2S_6$ the samples are easily damaged. The situation is rather complex since in our experiments the piezoelectric effect is not caused by an external field but the second term in Eq. 2.11.
Since the elements of the tensors given in Eq. 2.11 are not completely known, the calculation of internal stresses due to temperature change is difficult. These stresses can be of importance for the explanation of the variation in the phase transition temperature.

2.3.2 Optical absorption

The symmetry of the lattice determines the symmetry of the properties. And since we have a monoclinic lattice, it is useless to speak of ordinary and extraordinary waves: there is not a single optical axis. Therefore all properties are expected to be orientation-dependent. Weak polychroism was reported by Hellwig [26]. The bandgap as the origin of the fundamental absorption is a lattice property and is likely to be affected by phase transitions. At room temperature it is approximately 2.3 eV ($\approx$ 540 nm), shrinks to 2.2 eV ($\approx$ 560 nm) for 330 K and drops to 2.1 eV ($\approx$ 590 nm) exceeding T_c. For low temperature the band gap increases to about 2.5 eV ($\approx$ 500 nm). This is visible for the naked eye. Samples cooled down in liquid nitrogen look faintly yellow instead of orange, a clear indication that green is transmitted whereas blue is still absorbed.

2.3.3 Electrical conductivity

The dark conductivity depending on pre-illumination and the photoconductivity was investigated by Grabar in 1995 [27]. Persistent conductivity occurs after exposure to white light at room temperature. The persistence can be destroyed by annealing to the paraelectric phase ($T > T_c$). It is not simply an effect of temperature, but the phase transition has a crucial role in this persistence. Without this annealing the persistent conductivity could still be ascertained several weeks later.
In reference [27] the conductivity is plotted versus T^{-1}. For temperatures exceeding about -30° C the conductivity increases. We shall return to this later but the correspondence to the observed slow compensating holographic grating that can be frozen at -30° C [2] is obvious.

Thermal expansion

The temperature dependence of the thermal expansion of $Sn_2P_2S_6$ along [1 0 0] and [0 1 0] is reported in [28][4]. Along [0 1 0] the coefficient of thermal expansion α_{TE} is about $8 \cdot 10^{-5}\,\mathrm{K}^{-1}$ at 270 K and decreases sharply above 310 K to almost zero. Along the vector of spontaneous polarization in the [1 0 0] direction α_{TE} is about $-2 \cdot 10^{-5}\,\mathrm{K}^{-1}$ at 270 K, remains almost unchanged to $\mathrm{T_C}$ and jumps to $6 \cdot 10^{-5}\,\mathrm{K}^{-1}$ above $\mathrm{T_C}$.

2.3.4 Photoelectret state

'Photoelectret state' in this context describes another metastable feature of $Sn_2P_2S_6$. After application of an external electric field or exposure to light a considerable internal electric field remains. In some samples of $Sn_2P_2S_6$ this field is estimated to be as large as $1 \cdot 10^5$ V/m [29]. In the photorefractive effect a deviation from the phase shift between the intensity pattern and the refractive index pattern of 90°, predicted for diffusion, was observed. This is an evidence of other charge driving forces. However, the origin of this photoelectret state is puzzling.

2.4 Microscopic properties

Band structure

I.V. Kityk et al. were the first to publish a band calculation as well as an electron energy spectrum [30]. Some of the bindings could be experimentally identified by x-ray photoemission spectroscopy (XPS) [12]. Similar XPS measurements done in Osnabrück by B. Schneider in the group of Prof. M. Neumann confirmed these results.
Dr. A. Postikov from the University of Duisburg, Germany, performed 'tight binding linear muffin tin orbital' (TBLMTO) calculations of $Sn_2P_2S_6$ based

[4] The directions refer to the unit cell chosen by [15]

on the structural data of [15]. By convention the maximum energy value of valence states is zero, thus all negative values refer to valence band states while for positive values the band gap is followed by conduction band states. The following density of state calculation are a courtesy of A. Postnikov. The density of states is given in arbitrary units, nevertheless the scales are corresponding.

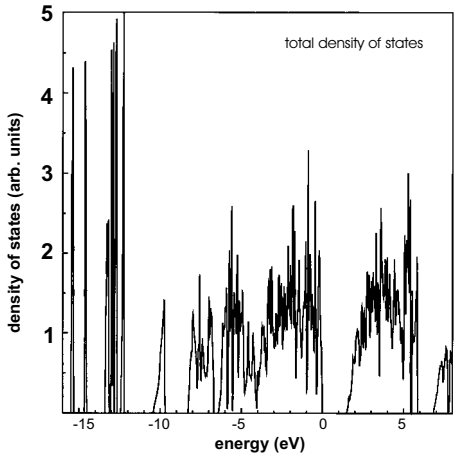

Figure 2.4: *Total density of states in $Sn_2P_2S_6$ obtained from TBLMTO calculation.*

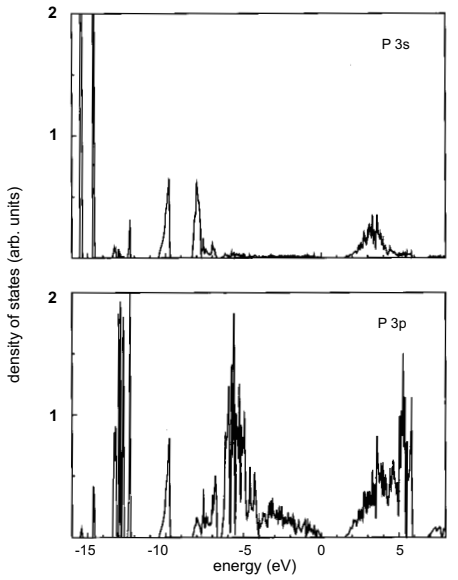

Figure 2.5: *Density of states of phosphorus in $Sn_2P_2S_6$. There is only little density of states for the valence band and some for the conduction band.*

2.4.1 Bond structure

Becker et al. [31] discussed the character of the bindings in the $(P_2S_6)^{-4}$ anion of $Pb_2P_2S_6$. They conclude that the P-S binding has considerable π-character.

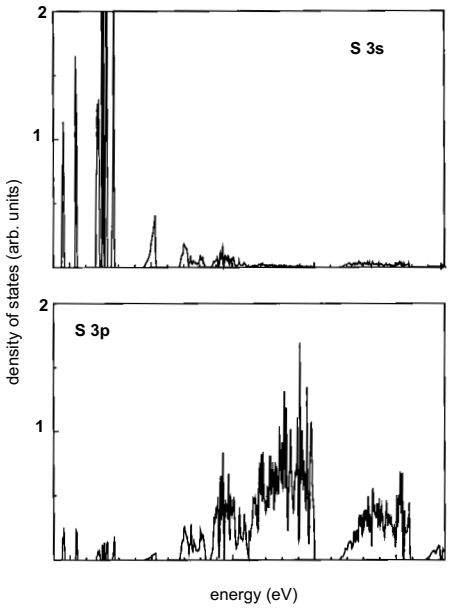

Figure 2.6: *Density of states of sulfur in $Sn_2P_2S_6$. The valence band is mainly provided by S 3p states. There is little contribution to the conduction band.*

The analogy to $Sn_2P_2S_6$ is likely for two reasons:

- the Raman-spectra of the $(P_2S_6)^{-4}$ are almost identical in both cases
- $Pb_2P_2S_6$ and $Sn_2P_2S_6$ are isostructural

Because of its reactivity, P^{4+} will not occur. Much more probable is a fluctuating shift of one electron between both phosphorus ions, intermediately creating P^{3+}-P^{5+} as a limiting state where both phosphorus have a complete shell. This will be triggered by a faint asymmetry in the electronegativity of the vicinity.

2.4.2 Charge carriers

A very elegant way to determine the charge carrier sign is the non-steady-state photoelectromotive force (photo-emf), introduced by Petrov et. al [32]. The investigation of $Sn_2P_2S_6$ with this method [8] clearly identified p-type conductivity as dominant. [5] In holographic measurements, other compensating gratings are reported [2] that indicate the presence of comparatively slow negative charge carriers [6] .
$Sn_2P_2S_6$ has comparably large dielectric tensor elements and pyroelectric coefficients. Both properties indicate a soft lattice that can be attributed to the freedom of tin to move with respect to the (P_2S_6)-unit.

[5] Unfortunately the authors do not explicitly mention whether the samples were pre-exposed to band-band excitation or not.

[6] The product μN, with the charge carrier mobility μ and the number of negatively charged carriers N is small.

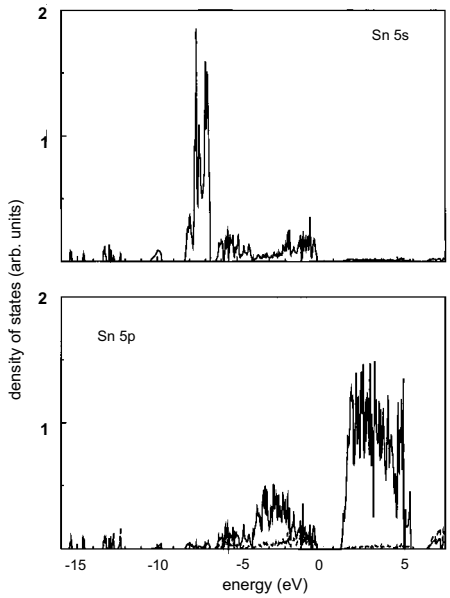

Figure 2.7: *Density of states of tin in $Sn_2P_2S_6$. Comparison with Fig. 2.4 illustrates that the conduction band mainly consists of Sn 5p states.*

A few words about polarons: If a lattice is easily polarized by ionic displacements, a condition that is fulfilled in almost all photorefractives, charge carriers can induce a lattice deformation. This lattice deformation results in a reduction of the electronic energy. Depending on the range of this deformation, large (several unit cells), intermediate and small polarons (single unit cell) can occur. Near a defect the trapping can even result in a bound small polaron.

Chapter 3

Methods

While most spectroscopic methods of solid state physics are insensitive to defects in low concentration, Electron Paramagnetic Resonance (EPR) is able to detect paramagnetic defects in ppm concentration, the typical order of magnitude for photorefractive sensitization.
Optical absorption is the key for photorefractivity because it makes the photons work. We detect absorption changes in order to trace the light induced charge transfer paths and employ combined EPR-optical absorption spectroscopy to assign optical absorption bands to microscopic defects.
Luminescence, no matter if photo- or thermally stimulated, gives insight to the thermal defect levels, different from the optical levels (see Fig. 3.3).

3.1 Optical absorption

Whenever photons[1] are absorbed, energy is partially dissipated resulting in a heating of the sample. In $Sn_2P_2S_6$ the band gap is very sensitive to temperature changes around 295 K (see chapter 2). Figure 3.1 illustrates the appearance of an absorption band for detection of absorption changes.
We can briefly estimate the contribution of the shrinking band gap if the sample is heated by absorption: Typical values of a few mW probe light power, the specific heat capacity $c_p(290\ K) = 230\ \frac{J}{mol\ K} = 468\ \frac{J}{kg\ K}$ [33], a typical volume of $1 \cdot 2 \cdot 2\ mm^3$ and a density of $\rho = 3.54 \frac{g}{cm^3}$ [15] result, according to:

$$\Delta T = \frac{\Delta E}{c_\mathrm{p}} \tag{3.1}$$

in a ΔT of several ten Kelvin. In equation 3.1 T denotes the temperature, ΔE the absorbed energy and c_p the heat capacity. This estimation is somewhat crude since all heat conduction is neglected.

[1] In the subsequent chapters we shall refer to light energies in units of 'electron volt': $E = \frac{hc}{\lambda} \Rightarrow 1eV = 1.602 \cdot 10^{-19} J \hat{=} 1240\ nm$

Measurements of the sample temperature depending on illumination were carried out. A halogen light bulb with a quartz light guide was used to reproduce the sample preparation as described by Hellwig [34] in order to photosensitize the sample. A sample in thermal contact with a thermal resistance PT100 showed a ΔT of about 12 K in the steady state.

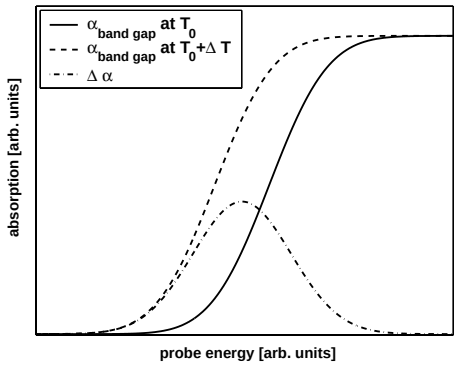

Figure 3.1: *An additional absorption band may be pretended by a shrinking or expanding band gap. The curves represent absorption data and the saturation has no physical meaning; it corresponds to the limited dynamic range of each spectrometer. Of course this situation can occur vice versa: An absorption band close to the fundamental absorption can pretend a smaller band gap.*

3.1.1 Two channel spectrometer

Optical absorption measurements are carried out with a two-channel spectrometer 'Bruins Omega 10' in transmission geometry. The major advantages of this setup are the high dynamic range and the comparably wide energy range from 0.5 eV to 4 eV [2]. The decisive drawback is the incompatibility with the EPR setup. Kinetics can only be followed at a single, fixed wavelength. All data are available in ascii format.
Absorption coefficients are calculated according to *Lambert-Beer's* law:

$$I(d,\lambda) = I(d=0,\lambda)e^{-\alpha(\lambda)d} \tag{3.2}$$

$$\Leftrightarrow \alpha(\lambda) = ln\left(\frac{I(d=0,\lambda)}{I(d,\lambda)}\right)d^{-1} \tag{3.3}$$

Here $I_{(d=0,\lambda)}$ denotes the intensity in front of and $I_{(d,\lambda)}$ the intensity behind the sample. The absorption coefficient $\alpha(\lambda)$ is usually given in units of cm^{-1}, the thickness d is therefore given in centimeters. The absorption coefficients are not corrected for reflection losses.

3.1.2 Optical Multichannel Analyser

The Optical Multichannel Analyser was developed to overcome the drawbacks of the Bruins Omega 10 and to meet the following requirements:
1) detection of small absorption changes, 2) rapid scanning, 3) high temporal

[2] 2400 nm to 300 nm in 0.1 nm resolution

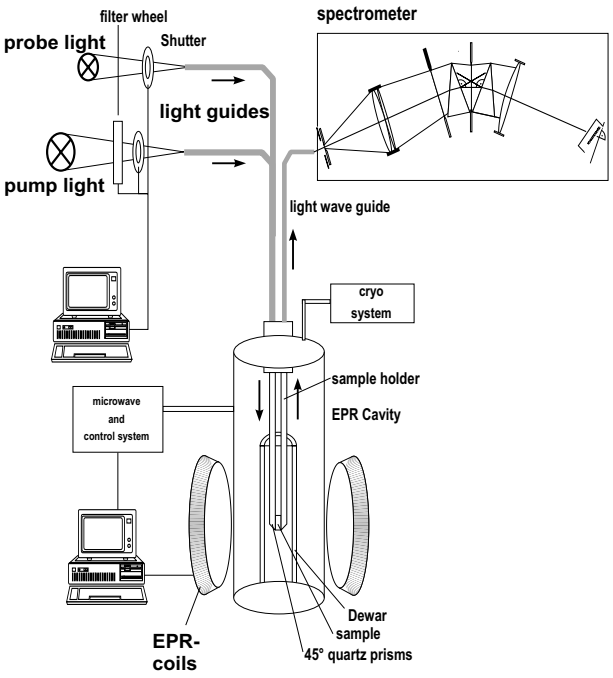

Figure 3.2: *The combined EPR-optical absorption setup. EPR and optical components can be used separately. In addition to the illustrated sample holder a room temperature sample holder was developed to avoid the losses inevitably connetected with the use of quartz rods. The cryo-system works between 4.2 K and 295 K.*

stability and 4) compatibility with the EPR device. For a detailed description refer to [35].

Since all measurements are done in transmission configuration and the absorption changes are expected to be rather small, a high dynamic range is required. Within this thesis, data of two different devices are used, OMA II and OMA IV, indicating consecutive steps of experimental optimization. The intermediate OMA III was based on a blazed grating as dispersive element and never met the requirements of the signal-to-noise-ratio (SNR) or temporal stability since the optimum wavelength of a blazed grating ranges from $\frac{1}{2}\lambda_{blaze}$ to $\frac{3}{2}\lambda_{blaze}$ [36]. We observed strong noise for both small and large probe energies. The emission of the probe light needs to be smooth in energy and stable in time, otherwise slight instabilities yield an immense signal in the quotients of intensity (see Eq. 3.3); consequently a halogen bulb with a smooth emission is used. However, a halogen bulb has hardly any UV emission for $\lambda < 400\ nm$ and enhancement of the UV emission can only be achieved by an increase of the bulb temperature, which results in an undesirable shortening of its lifetime (a 2% higher temperature halves the lifetime [37]). The complementary access to decrease the red spectral maximum at the detector is to relatively enhance the UV spectrum. This is done with a SCHOTT blue glass filter (BG 14), that shows no light induced absorption itself. All light guides are made of 'SUPRASIL' quartz with low absorption for $\lambda > 300\ nm$.
Since pump light needs to be intense to cause large absorption changes and

sequence	λ [nm]	energy [eV]
1	2500	0.496
2	1900	0.653
3	1420	0.873
4	1060	1.170
5	950	1.305
6	850	1.459
7	750	1.653
8	700	1.771
9	600	2.066
10	550	2.254
11	500	2.480
12	470	2.638
13	430	2.884
14	400	3.100
15	370	3.351
16	350	3.543
17	320	3.875

Table 3.1: Energy and wavelength for the transmission maximum of the used set of interference filters. HMFW is 10 nm for $\lambda < 1000$ nm, 20 nm for the others.

narrow-banded to obtain a good energetic resolution, the first idea is to make use of laser diodes. Unfortunately the availability of laser diodes in energetically equidistant steps is not yet assured. Therefore we use a xenon arc lamp with 150 W, attenuated and monochromized by a set of interference filters.

Attenuation of the output intensity of the xenon lamp is inevitable in order to prevent destruction of the highly absorbing filters. Thus it is not surprising that the intensity at the sample position is of the order of a few mW/cm^2 only. For critical energies laser diodes are available:

- 1.22 eV (1020 nm) with 500 mW
- 1.46 eV (850 nm) with 500 mW
- 1.85 eV (670 nm) with 30 mW

The detection system (see Fig. 3.2) consists of a slit, a set of lenses, two flint glass prisms acting as dispersive elements and a silicon photo-diode-array (PDA) from ANDOR. A slit allows to regulate the intensity over a wide range. The spectral sensitivity certainly suffers from the widening of the slit but the width of the absorption bands in $Sn_2P_2S_6$ is much larger than the resolution limit of the system. Light polarization is totally disregarded in all experiments.
Our complete setup is remotely controlled by a 32 bit program, developed by C. Veber, running under Windows NT.

Since we detect changes in transmission that are usually small, we need a high dynamic range, 10 bit for OMA II, 16 bit for OMA IV. We can only make use of the whole dynamic range if the intensity transmitted through the crystal

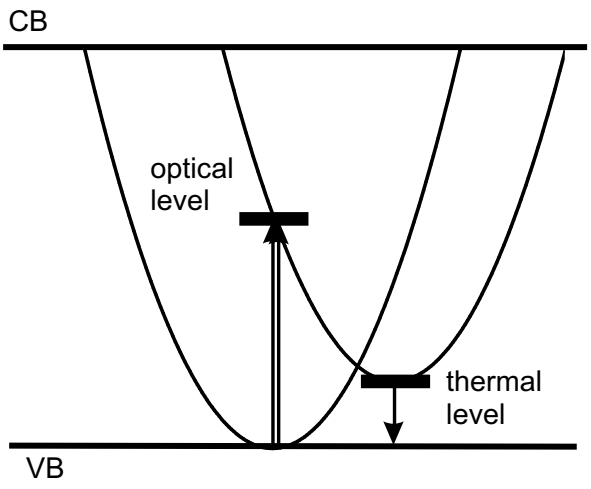

Figure 3.3: *Difference between thermal and optical energy levels. CB denotes conduction band, VB valence band. Two coordinate systems are superimposed. Band edges are in real space while the parabolae represent the dependence of elastic energy in configuration coordinates. The primary process, i.e. the initial excitation induced by light, is conventionally indicated by double arrows.*

is close to the maximum of the dynamic range. The relative change of transmission will be the same, no matter how much light we have on the detector, but the total change of counts depends on how much light we transmit absolutely. This is a dilemma, since the probe light itself induces changes of the defect charges. It has to be as weak as possible but as strong as necessary. Since the total detected energy $(I \cdot t)$ determines the signal level it is no use to decrease the probe light intensity and to prolong the integration time.

The common procedure to detect pump energy dependent changes of absorption is therefore to determine the optimum integration time for the specific situation first. This depends on the sample, the sample holder, the temperature and some subtleties such as the state of the sample i.e. domains etc. The sample is exposed to probe light and the optimum integration time is calculated from the transmitted light. This procedure inevitably causes exposure of the samples to probe light for several seconds. It has to be repeated whenever the optical beam is changed. In some cases an effect of such sensitization cannot be excluded.

Looking for absorption changes we need a reference that enters into Eq. 3.3 instead of $I(d = 0)$. This reference is the transmitted intensity of the crystal in its initial state without pre-exposure to pump light (but to some probe light: see above). It is important to emphasize that detail since in $Sn_2P_2S_6$ it is unknown how much totally absorbed energy is required to cause light induced metastability.

Next, starting with the lowest pump energy (see Tab.3.1), the samples are excited with monochromatic light for 60 s to achieve a dynamic equilibrium of excitation and recombination close to saturation. In most cases the assumption of a steady state after 60 s is fulfilled. Here we see that to some extent this method is time resolving because each exposure to a specific wavelength has a defined duration (of typically 60 s).

In $Sn_2P_2S_6$ the band gap limits the range of possible absorption changes. We can neither expect the high energy pump light to penetrate deeply into the bulk nor probe light with $E_{probe} > E_{gap}$ to pass through the sample to be detected. The detected optical absorption changes are caused by light induced changes of the defect concentration [35]. In $Sn_2P_2S_6$ such changes in concentration can occur by intervalence transfer and charge transfer. These effects change the defect charge state and consequently the optical absorption and paramagnetic properties. If our increasing pump energy becomes large enough to change the population of a defect state, either by excitation of charges to or from this state, the respective absorption will decrease since the origin of absorption is diminished. We therefore expect a light induced transparency at identical pump and probe energies, called a 'primary process'. This is why the pseudo-3D colormaps (see e.g. Fig. 4.13) include a diagonal along identical pump and probe energies. The transferred charges recombine leading to an increase of absorption of another defect level. These effects, called 'secondary process' necessarily take place off the diagonal.
Band-band excitation creates free electrons and holes in comparably large amounts and these charges can as well be captured by defect levels changing their charge state.
Optical excitation is governed by the Franck-Condon-principle, the theory of optical transitions respecting the Born-Oppenheimer-approximation. Optical excitation of electrons are too fast for the lattice to react. This is represented by vertical arrows in configuration coordinates (see Fig. 3.3).

3.2 Electron Paramagnetic Resonance

For a complete introduction to EPR, especially in solids, refer to [38, 39]. The subsequent section will only sketch the basics that concern $Sn_2P_2S_6$. An overview of the experimental setup is given in the lower part of fig. 3.2.
All EPR experiments discussed in this thesis were carried out at approximately 9.8 GHz, i.e. X-band, with a commercially available Bruker ER 200 D-SRC spectrometer and a cylindrical WZ cavity with large axial access. That cavity allows combination with a homemade sample holder consisting of two semi-cylindrical and EPR-silent quartz rods of 15 cm length. This setup permits simultaneous illumination of the sample during EPR measurements as well as OMA measurements (cf. section 3.1.2) at low temperatures.
The sample dimensions for EPR are limited by the cavity aperture to about 3 mm × 4 mm × 4 mm.

To demonstrate the principle of EPR (Fig. 3.4) we consider a system with orbital angular momentum l=0 and spin angular momentum s=1/2, m_s=± 1/2. Such a system is described by a Hamiltonian:

$$\mathcal{H} = -\mu_B g_0 \hat{s}_z B \tag{3.4}$$

with the Bohr-magneton $\mu_B = \frac{|e|\hbar}{2m_e}$, $g_0 = 2.0023$ of the free electron and $\hat{s}_z$: the

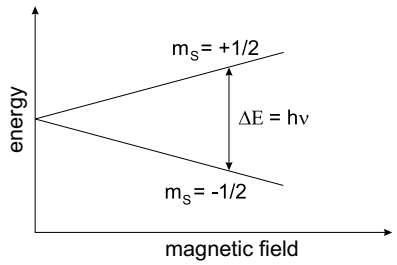

Figure 3.4: *Under an external magnetic field the degenerated Zeeman levels of $m_s = \pm 1/2$ are splitting according to equation 3.5*

z-component of the the spin-operator $\vec{s}_z$. $\mathcal{H}$ acting on $\hat{s}_s, |m_s\rangle$ with $m_s = \pm 1/2$ results in a difference of eigenvalues:

$$\Delta W = g_0 \mu B \tag{3.5}$$

corresponding to microwave energies for available laboratory magnetic fields. The principle of absorption is illustrated in Fig. 3.4.
The situation given in Eq. 3.4 describes the trivial case of an isolated single spin in a magnetic field. Generally, the situation of EPR in a crystal is more complex and requires a Hamiltonian that takes into account $\vec{L}\vec{S}$-coupling, hyperfine interaction and the crystal field.
$\vec{L}\vec{S}$-coupling introduces excited states to the ground state, assuming zero expectation value of angular momentum initially:

$$g = 2.0023 - a\frac{\lambda}{\Delta} \tag{3.6}$$

where λ denotes the coupling constant ($\propto Z^4$), Δ the energy difference between ground and excited states and a the admixture of excited orbital states.
The orientation dependence of g, i.e. the orientation dependence of the Zeeman-splitting, is due to the fact that the admixture of excited orbital states depends on the relative orientation of the defect axes to the magnetic field. We thus arrive at a real second rank tensor for g.
The general Hamiltonian is:

$$\mathcal{H}_S = \mathcal{H}_z + \mathcal{H}_{hf} + \mathcal{H}_{cf} \tag{3.7}$$

where $\mathcal{H}_z$ denotes the Zeeman-part of the spin-Hamiltonian for $\vec{L}\vec{S}$-coupling, $\mathcal{H}_{hf}$ denotes the hyperfine Hamiltonian and $\mathcal{H}_{cf}$ the Hamiltonian of the crystal field.
Often, also in $Sn_2P_2S_6$ the detection of EPR at room temperature is impeded, mainly due to spin lattice relaxation.

3.2.1 Photo-EPR

In order to observe simultaneous changes of optical absorption as well as EPR, we make use of a special sample holder that is neither photochromic nor param-

agnetic. Two 'SUPRASIL' quartz rods with a 45° cut (see Fig. 3.2), acting as sample holder as well as light guide, allow to combine the Optical Multichannel Analyzer with the EPR device from 4.2 K to 295 K. The intensity of an EPR signal is plotted versus pump energy (typically 17 discrete values according to Tab.3.1) and compared to the change of optical absorption at a specific probe energy (also as a function of pump energy).

3.3 Luminescence

To detect thermally stimulated luminescence [40] the specimens are exposed to band-band-excitation[3] at low temperature. Metastabely trapped carriers in shallow traps can then be thermally ionized under heating.
Although not all released carriers cause luminescence but recombine without radiation the number of thermally excited carriers is proportional to the intensity of luminescence. Arrhenius' law describes the thermal release of charge carriers:

$$I(T) \propto n(T) \quad = \quad \exp\left(\frac{E_a}{k_b T}\right) \tag{3.8}$$

In order to determine the trap depth e.g. the initial slope of the emission can be evaluated.
All luminescence measurements were performed in cooperation with the lab of A. Kadashchuk at the Institute of Physics, National Academy of Sciences, in Kiev, Ukraine. They use a temperature controlled bath cryostat with 0.02 K tolerance ranging from 4.2 K to 295 K and a photomultiplier to detect the luminescence. Typical heating rates are about 0.2 $\mathrm{K\,s^{-1}}$.

3.4 Photoconductivity

The measurements are done with a set-up in the group of Prof. E. Krätzig at the department of physics in Osnabrück. Monochromatic light is provided by a grating monochromator that needs to be protected from the intense IR emission of the light source by an aqueous $CuSO_4$ solution. Therefore the complete setup is limited to a spectral range from 400 nm to 780 nm (3.10 eV to 1.59 eV).
Since the device allows the detection of the spectral intensity, it is possible to measure the *specific* photoconductivity σ^s_{ph}:

$$\sigma^s_{ph}(\lambda) = \frac{\sigma_{ph}(\lambda)}{I(\lambda)} \tag{3.9}$$

$$\tag{3.10}$$

with

$$\sigma_{ph}(\lambda, I) \quad = \quad qn(\lambda, I)\mu \tag{3.11}$$

[3] 436 nm (2.84 eV) line of a mercury-lamp

Here q is the charge, μ denotes the effective mobility [4] and n is the number of charge carriers that primarily depends on the intensity and only secondarily on the excitation energy.
In the range of the applied electric field the response needs to be ohmic. Otherwise the measured current is no longer an appropriate indicator of the conductivity and implicitly the number of released charges. This needs to be checked before any other measurement is carried out.
Furthermore the transient currents such as photovoltaic and pyroelectric currents have to relax until the steady state value is determined. Investigation of the photovoltaic tensor was performed by Hellwig [34].

[4] The mobility $\frac{v}{E}$ refers to moving charge carriers only. In materials with a lot of shallow traps the charge carriers are trapped most of the time and only moving when they are thermally ionized. An experimental way to separate the (actual) mobility from the effective mobility by Hall measurements was presented by Ohmori et al. [41].

Chapter 4

Results

The methods introduced in chapter 3 were applied to the different samples listed in table 4.1. Not all of them were suitable for every method; we will have to keep this in mind for the interpretation of data and their generality.

4.1 Optical absorption

As mentioned, the initial state of the samples is difficult to define as long as it is unknown which deposited energy is sufficient to photosensitize the material persistently. We took special care not to expose the samples to light. They were kept and mounted in the dark until the measurements were done.
For the optical absorption measurements with the two-channel spectrometer typically 16 measurements are averaged to improve the signal-to-noise-ratio. In general, nominally pure samples are orange and become yellowish when cooled down to 77 K. Neither the color of iron doped samples nor of selenium doped material can be distinguished from the nominally pure samples by the naked eye. Sometimes we find small regions close to the edges of orange samples that

name	dimension (mm × mm × mm)	comment
K3	3,4,1	fragment, nominally pure, type I
K2	8,2,2	nominally pure, type II
N4	5,4,4	nominally pure
SPS 12	7,3,3	nominally pure
New1	4,3,3	nominally pure
SPS:Se	3,3,1	0.5 wt% Se
SPS:Fe	3,3,2	0.5 wt% Fe, fragments
old dark	3,2,1	fragments
new dark	5,4,3	nominally pure

Table 4.1: List of available samples and their dimensions.

look similar to the brownish 'dark' $Sn_2P_2S_6$ but these parts were never large enough to do optical absorption spectroscopy with them.
The measurements of optical absorption can be impeded due to scattering by internal cracks that can also contribute to extinction [1]. The position of the absorption bands is therefore of more interest and more reliable than the absolute value that may be slightly misleading since relative shifts of 20-30% have to be taken into account.
Nevertheless the data are representative of the respective class of material they are attributed to. All optical absorption measurements are done at 295 K with samples with at least two parallel and polished surfaces. Polarization dependent effects, i.e. polychromism, were not investigated.

Nominally pure $Sn_2P_2S_6$

$Sn_2P_2S_6$ shows a fundamental absorption at about 2.3 eV. As expected, in nominally pure samples there is only a weak absorption below this energy. Fourier-IR spectroscopy in the range of 0.15 eV to 1 eV revealed no evidence for further absorption bands in the near IR [42].

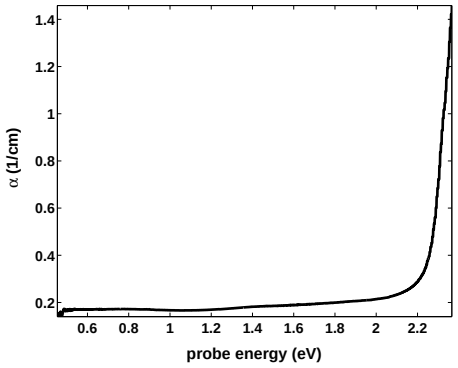

Figure 4.1: *Optical absorption of nominally pure $Sn_2P_2S_6$ (New1) . There is only very weak absorption below the fundamental absorption edge. Enhancement of the range below the band gap shows that these absorptions are at the same position as shown in Figs.4.2,4.3.*

$Sn_2P_2S_6$:Fe

Figure 4.2 shows two different absorption bands in a sample of $Sn_2P_2S_6$ doped with 0.5 wt % iron in the starting materials: a faint one at about 0.8 eV and another wide one starting at 1.2 eV that overlaps with the fundamental absorption. The overall absorption of the sample is higher than of the nominally pure sample, an effect that may be caused by scattering.

[1] $I_{Reflection} + I_{Extinction} + I_{Absorption} + I_{Transmission} = I_0$; extinction (any kind of intensity loss except absorption inside the sample) and absorption cannot be separated by our setup.

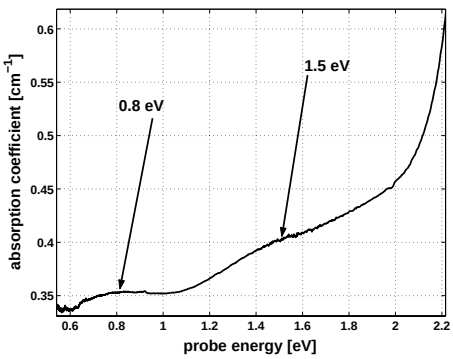

Figure 4.2: *Optical absorption of $Sn_2P_2S_6$:Fe. Two absorption bands can be distinguished: at 0.8 eV (1550 nm) and another one starting at 1.2 eV (1025 nm). The latter is overlapping with the fundamental absorption; so possibly further absorptions between 1.5 eV and 2.3 eV cannot be resolved. The comparatively large background absorption values are likely to result from extinction by cracks: it is rather independent of wavelength since the sample is orange as well and does not look dark.*

$Sn_2P_2S_6$:Se

The selenium doped samples are rectangularly cut, polished and of good optical quality. As shown in Fig. 4.3 this material has comparatively low absorption below the band gap.

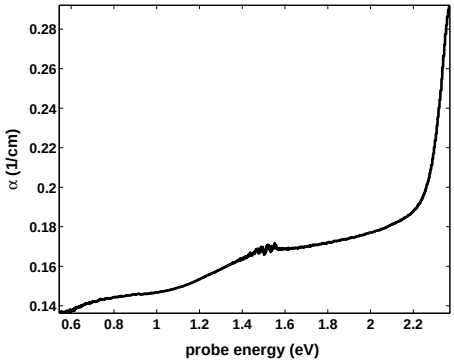

Figure 4.3: *Optical absorption of $Sn_2P_2S_6$:Se. Although on a much smaller level, the absorption bands of $Sn_2P_2S_6$:Se are identical with what is observed in $Sn_2P_2S_6$:Fe in a much more pronounced way. Noise at about 1.5 eV is an artifact.*

Dark $Sn_2P_2S_6$

As indicated by the commonly used expression, 'dark' $Sn_2P_2S_6$, the absorption is larger than in usual samples. An absorption spectrum of dark $Sn_2P_2S_6$ is shown in Fig. 4.4. It is in good agreement with the data published by Grabar et al. [9].

Comparing nominally pure, iron- and selenium-doped samples, it turns out that the absorption bands are at the same position but of different intensity. In intentionally iron doped $Sn_2P_2S_6$ both absorption bands are rather intense, especially the one at about 1.5 eV, whereas selenium does not yield a unique absorption.

In contrast the dark $Sn_2P_2S_6$ has a much higher absorption and an additional

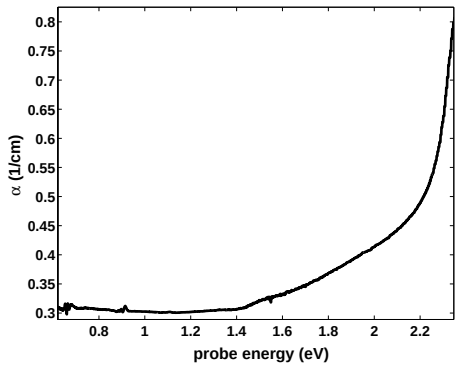

Figure 4.4: *Optical absorption of 'dark' $Sn_2P_2S_6$. A strong absorption band is overlapping with the fundamental absorption.*

absorption starting at 1.4 eV that possibly consists of different single bands and that strongly overlaps with the fundamental absorption.

4.2 Light induced optical absorption changes

The data presented in the following section were obtained after direct exposure of the samples to the complete spectrum of the xenon lamp focussed onto the sample. This intense illumination was used to see whether an additional absorption band occurs that cannot be obtained by the comparably faint transmitted light of the interference filters used in the OMA setup.

4.2.1 Measurements at room temperature

After 60 s of intense white illumination at 298 K, comparable to what is used to photosensitize the samples for infrared recording, a single spectrum of the absorption change is measured with a delay of less than 200 ms.
All measurements show the same absorption feature around probe energies of 2.2 eV to 2.4 eV. This peak results from the heating of the sample according to equation 3.1 and Fig. 3.1 because illumination with white light heats the sample considerably. Since this results in a shift of the band edge towards lower energies we cannot interpret the described absorption as defect-related. Apart from this 'pseudo'-absorption near the band edge, nominally pure $Sn_2P_2S_6$ (New 1) does not show any further light induced absorption changes. This is different in all other investigated undoped $Sn_2P_2S_6$ samples, as shown in Figs. 4.6, 4.7 and 4.8.

Other nominally pure samples show a different behavior. Sample 'SPS 12', as illustrated in Fig. 4.6, exhibits an increase of absorption around 1.9 eV after band-band excitation at room temperature.

This absorption around 1.9 eV is almost the same as in another nominally pure sample 'N4', shown in Fig. 4.7. Sample 'K3' in Fig. 4.8 shows almost the same change of absorption as samples 'SPS12' and 'N4'. The small increase of absorption at probe energies of 1.2 eV is very small and just beyond the

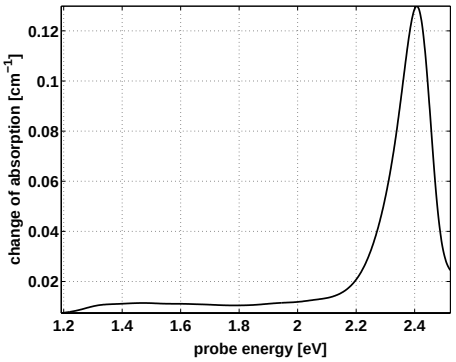

Figure 4.5: *Change of absorption of a nominally pure sample (New1) after intense illumination with white light at 298 K. As well as in the subsequent line plots the narrow and pronounced absorption band around 2.3 eV originates from an absorption and consequently temperature-induced shrinking of the band gap.*

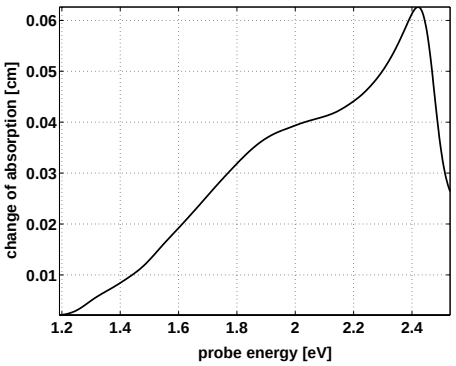

Figure 4.6: *Change of absorption of a nominally pure sample (SPS12) after intense illumination with white light at 298 K. The width of absorption bands in $Sn_2P_2S_6$ is considerable. They are about as wide as those in oxides indicating a comparably strong electron-phonon coupling.*

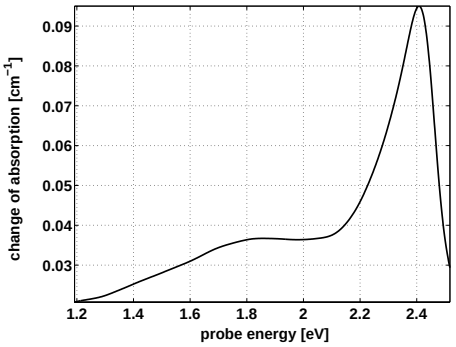

Figure 4.7: *Change of absorption of a nominally pure sample 'N4' at 298 K.*

experimental error. This change of absorption is unique for sample 'K3'. Although this signal is very weak and at the limit of sensitivity of our OMA IV, it is certain that it is not persistent, but decays faster than the band at 2.0 eV. Concluding we see that most of the nominally pure samples show a significant change of absorption of comparable size around 1.8 eV.

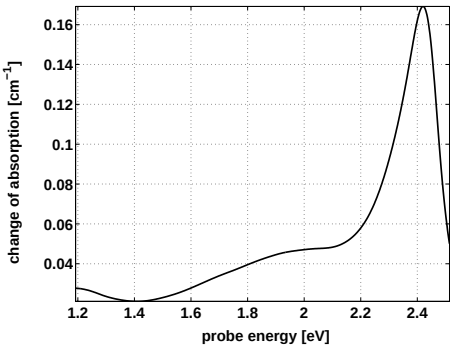

Figure 4.8: *Sample 'K3' shows a light induced absorption at about 1.8 eV like other nominally pure samples. There is another very faint increase of absorption around 1.2 eV.*

$Sn_2P_2S_6$:Fe

We remember that the absolute absorption coefficients are comparably large in iron doped samples. Figure 4.9 shows how the total absorption of this sample changes after intense band-band excitation.

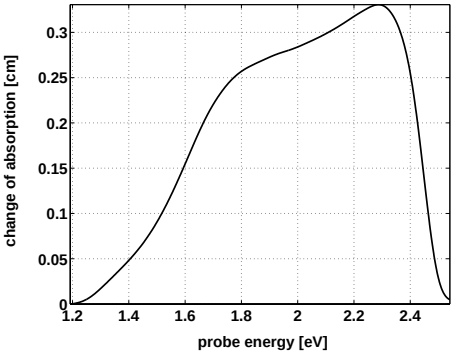

Figure 4.9: *The change of absorption at 1.8 eV in intentionally iron doped material is about five times larger than in nominally pure samples. Since the sample has a higher absorption, the heating is stronger than in nominally pure samples, as a consequence the absorption caused by the shrinking band gap is larger and shifted towards lower energies.*

First, in intentionally iron doped samples, there is a pronounced change of absorption at about 1.8 eV. Second, the total absorption is increased, leading to a strong heating and consequently to a larger 'pseudo'-absorption at 2.3 eV.

$Sn_2P_2S_6$:Se

Selenium doped samples are weakly absorbing below the band gap (see Fig. 4.3). Figure 4.10 illustrates that there are almost no changes of absorption after intense band-band excitation at room temperature.

Dark $Sn_2P_2S_6$

From the previous measurements we expect a stronger shift of the band gap by heating due to the large absorption of the 'dark' sample. At least Figs. 4.9 and 4.11 confirm this. In contrast to the other samples presented so far, there is no clear absorption band below the band gap but rather a wide absorption

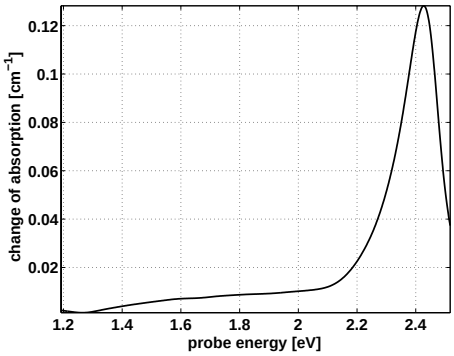

Figure 4.10: *$Sn_2P_2S_6$:Se with no significant change of absorption below the band gap.*

structure. Since the slope is almost constant it is difficult to figure out any individual absorption band, though at about 1.6 eV and 2.0 eV there seem to be shoulders indicating two distinct absorption structures.

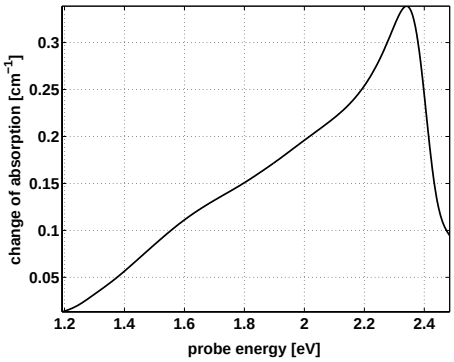

Figure 4.11: *The new 'dark' sample that was grown under definite conditions shows a very wide absorption below the band gap. A closer look reveals two shoulders at about 1.6 eV and 2.0 eV. The absorption coefficient given in Fig. 4.4 corresponds to this sample.*

The major difference between both dark samples ('old' and 'new') is that they might have been grown under different conditions. While the first dark $Sn_2P_2S_6$ specimen shown in Fig. 4.11 was grown under definite conditions given in the Appendix, the dark $Sn_2P_2S_6$ in Fig. 4.12 was unintentionally grown under conditions that could not be purposely reproduced until recently [9]. But nevertheless the result seems to be different. The change of the optical absorption of the first dark $Sn_2P_2S_6$ specimen resembles much more that of the iron doped material than the new dark one.

The changes of absorption usually depend on the pump energy. In order to determine the spectral dependence of light-induced absorption changes we use monochromatic light with increasing energies as given in table 3.1.
Commonly changes of absorption are presented as shown in the lower part of Fig. 4.15. This presentation has the major disadvantage that no sequence of the signals involving the excitation energy can be given. To overcome this problem we use pseudo-3D colormaps. For illustration see, e.g., Fig. 4.13.
Absorption changes are represented by color, encoded according to the colorbar

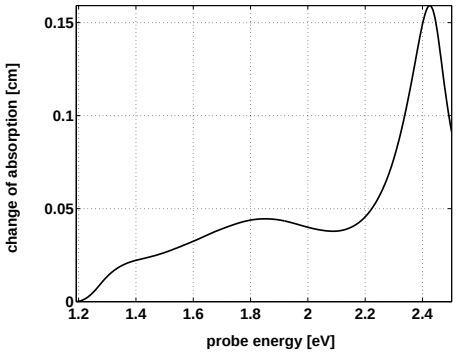

Figure 4.12: *Change of the optical absorption of the $Sn_2P_2S_6$, unintentionally turning out to be dark after growth. Apart from a small increase of absorption around 1.4 eV the change of absorption is similar to the nominally pure samples 'SPS 12' and 'N4'.*

to the right of the figures. Note that the absolute value of each color changes from measurement to measurement. Probe light energy is plotted on the abcissa while the pump light energy is plotted on the ordinate. Black lines in the graphs are contours of equal absorption change. The small red lines on the left side remind of the used excitation energies. Between these lines the data have been numerically interpolated. To eliminate noise, data along the abcissa are slightly smoothed.
A thin blue diagonal connects points of equal pump and probe energy (see e.g. Fig. 4.13). As mentioned above, this diagonal has an important meaning: primary processes take place along this diagonal. If a charge carrier is photoionized from a defect by a certain optical energy, this state will be depopulated and lose absorption at the same energy. Thus light induced transparency occurs along this line. All subsequent or secondary processes occur off this diagonal.

The subsequent section will compare, for both 295 K and 10 K, the effect of various pump light energies on a sample that was kept in the dark for several weeks and then excited metastabely by band gap illumination. The aim is to investigate the charge transfer properties of this metastable situation.

Nominally pure $Sn_2P_2S_6$

The light induced changes of absorption shown in Fig. 4.13 were obtained with sample K3 that was kept in the dark during several weeks before. In contrast to measurements with the two-channel spectrometer the samples do not need to have parallel and polished surfaces for measurements with the OMA spectrometer. Even wedge shaped samples like the K3 fragment or opaque materials with strong domain wall scattering can be used. They do not impede OMA measurements since only differences are monitored and all extinctions that are insensitive to light, will be eliminated by this procedure. Starting at low pump energies a transparency occurs in a narrow energy range, near 2.3 eV, close to the band gap. Considering the previous data we can attribute this to a cooling of

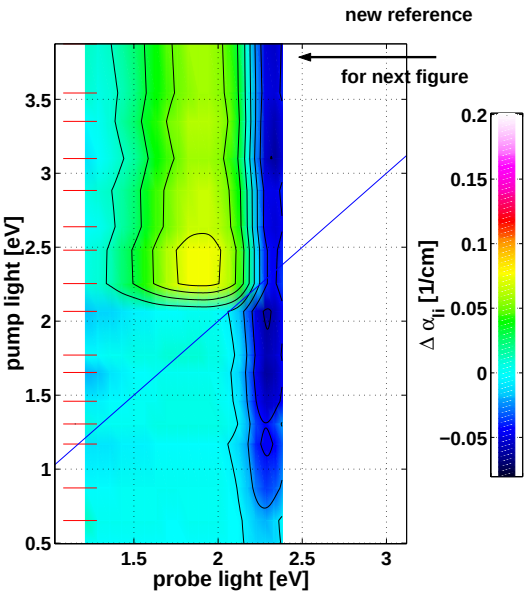

Figure 4.13: *Light induced change of absorption of a nominally pure sample 'K3' at 295 K depending on excitation energy. For probe light energies close to the band gap we see a transparency that cannot be attributed to a pump energy since it starts from the very beginning of the measurement. It results from the fact that the reference spectrum was, as usual, taken shortly after the determination of the optimal integration time. This caused a slight heating of the sample. During subsequent measurements with weak probe light the crystal cooled down again. As a consequence we observe a widening of the gap leading to a transparency around 2.4 eV. For band-band excitation a wide absorption occurs at about 1.9 eV. The steady state at the top of the figure is used as new reference for Fig. 4.14.*

the sample after excitation (see Fig. 4.13 and its caption) [2]. For pump energies close to and exceeding the band gap (2.3 eV at 295 K), a wide absorption band with a maximum at 1.9 eV occurs that remains unaltered for at least 20 min. Light energies exceeding the band gap cannot penetrate into the bulk and consequently cannot cause further absorption changes[3]. Since each excitation takes 60 s we know, counting the red lines at left in the figure, that between excitation with 2.3 eV and 4 eV about 6 min pass without any significant decay of the light induced absorption change.

It is worth mentioning that in $Sn_2P_2S_6$ light induced absorption changes at room temperature have not been reported before.

Corresponding measurements with $Sn_2P_2S_6$ have been performed before. Since Hellwig [34] was interested in the holographic sensitization, she always used the photosensitized crystal state as reference. Therefore she was never able to see the change of absorption, illustrated in Fig. 4.13, for a sample that is exposed to band-band excitation for the first time after being stored in the dark during weeks. Moreover, the better sensitivity of OMA IV compared to OMA I that she used, now allows us to detect the light induced absorption changes after

[2] Apparently the probe light to determine the optimal integration time was sufficient to cause a measurable heating.

[3] The light energy is still insufficient to cause irreversible defects.

photosensitization, using the sensitized state as a new reference. The obviously steady state after band-band excitation will not decay during the duration of a further measurement. Therefore it is possible to use it as a new reference to detect light induced absorption changes relative to this state. The experimental

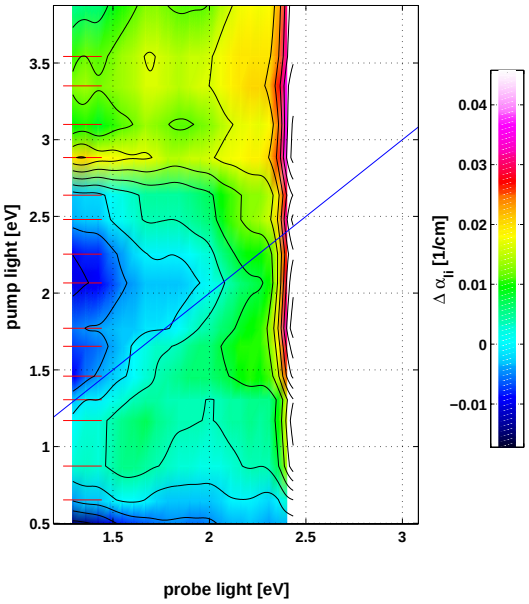

Figure 4.14: *Light induced change of absorption of a nominally pure sample 'K3' at 295 K after the measurement illustrated in Fig. 4.13. We used the final state there as reference for the change of absorption shown here, so all of the absorption changes given here are relative to this state. Therefore band-band excitation results only in a faint increase of absorption. For a pump energy of 1.3 eV (950 nm) we see a light induced transparency as well as a less pronounced one at 1.8 eV. No resulting secondary processes can be found. It is probably due to the low dark conductivity of K3 that these changes lasted long enough to be monitored.*

advantage is that the dynamic range of any presentation, either by colormaps or line-plots, is limited by what can be resolved on the background of a large signal. So after such a large signal occurred, that must not change, it is useful to take this signal as the new reference.
For all colormaps shown below we see that the relative changes of the metastabely excited crystal, no matter if at 10 K or 295 K, is about one order of magnitude smaller than the initial change of absorption for band-band excitation.

4.2.2 Low temperature measurements

At low temperature the recombination of trapped charge states is slowed down; so a higher level dynamic equilibrium of excitation and recombination can be achieved. Light induced absorption changes then are usually more pronounced, and some levels that are thermally ionized at 295 K are populated.

After the light energy exceeded E_{gap}, the samples are exposed to band gap excitation for a cumulated time span of several minutes, since every single excitation (small red lines at the ordinate side of Fig. 4.15) takes 60 s. This light, as mentioned above, does not penetrate into the bulk. As can be seen in Fig. 4.15 the resulting absorption changes do not decay. If the procedure is repeated,

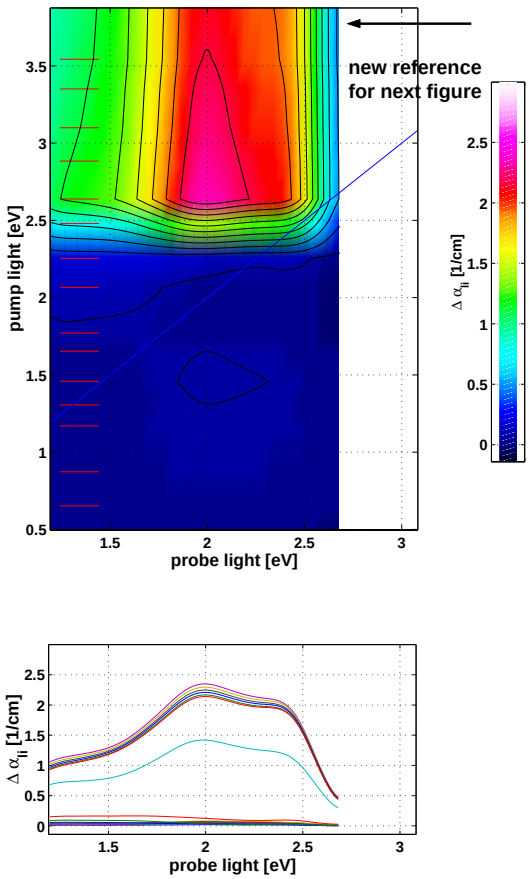

Figure 4.15: *Typical light induced absorption changes in undoped $Sn_2P_2S_6$ at 10 K. The sample had been stored in the dark during several weeks before. We proceeded in the same way as described above and used the final steady state here as a reference spectrum in Fig. 4.16.*

starting from low energies, charge transfers involving previously trapped charge carriers are possible.

An increase of the band gap by 0.2 eV at low temperature compared to 295 K is predicted and clearly confirmed by the dependence of the wide absorption on pump energy (Figs.4.14: threshold 2.3 eV and 4.16: threshold 2.5 eV). The strongest increase of absorption at low temperature is at 2.0 eV, though there are other bands at 1.5 eV and 2.2 eV, overlapping with the fundamental absorption. In figure 4.16 two primary processes are observed below the band gap, firstly a about 1.5 eV and secondly at about 2.0 eV. For excitation with 2.0 eV the absorption at 1.5 eV recovers; that means: a secondary process occurs.

What was measured in this way with all available samples including $Sn_2P_2S_6$:Se, is illustrated in Fig. 4.17: there is no significant difference to the nominally pure sample 4.16. Also the light induced absorption changes in $Sn_2P_2S_6$:Fe at 10 K look almost the same. Comparison of light induced absorption changes after photoexcitation at 10 K with 295 K shows two primary processes at about 1.5 eV and at 2.0 eV: both are shifted towards lower energies by about 0.3 eV

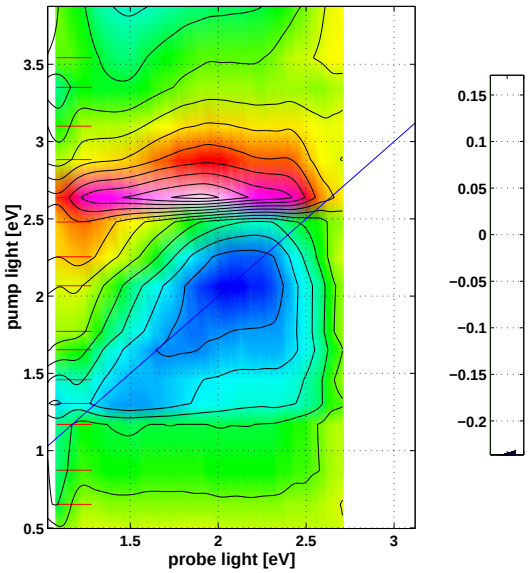
pump light [eV]
probe light [eV]
0.5
1
1.5
2
2.5
3
3.5
1.5
2
2.5
3
0.15
0.1
0.05
0
−0.05
−0.1
−0.15
−0.2

4.2.3 Temperature dependence

Heating of a sample that had been exposed to band-band excitation at low temperature leads to thermal ionization of charges captured in shallow traps and a subsequent change of absorption of the respective defect. Such investigations were carried out for the nominally pure sample K3 as illustrated in Fig. 4.18. Again, the change of absorption between 2.1 and 2.5 eV is due to the shrinking band gap.

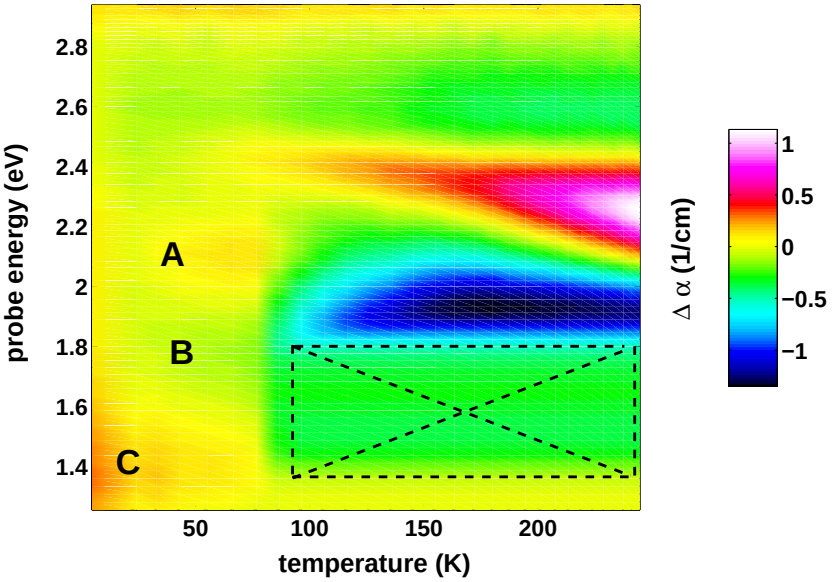

Figure 4.18: *Heating run with a nominally pure sample that was exposed to band-band illumination at low temperature. For temperatures above 80 K a pronounced transparency occurs below 2.0 eV that exceeds the dynamic range of the detector. It is therefore indicated by the hatched range. For such higher temperatures we also see the shrinking of the band gap. As expected there is a strong absorption, shifting towards lower energies (see Fig. 3.1). Two smaller absorption bands for temperatures below about 80 K are indicated A and B. They are illustrated in more detail in Fig. 4.19.'C' denotes a third absorption band.*

For temperatures below about 80 K a charge transfer from one defect to another one is observed under rising temperature indicated by the changing intensities of the features labelled A,B and C. Figure 4.19 presents the change of these optical absorptions for a heating experiment at different temperatures. While the absorption at 1.8 eV (B) decreases with temperature, the absorption band at 2.1 eV (A) increases. The existence of a point of constant $\Delta\alpha$ indicates a light-induced reaction governed by a single arrow. There is a third absorption

band (C) at about 1.4 eV that slowly decays with increasing temperature.

For temperatures exceeding 100 K the sample becomes transparent over the whole detected range below the band gap as indicated by the hatched area. This feature is unexplained. At almost the same temperature Iwata et al. report a peculiarity of the dielectric dispersion [43] that they attribute to a structural reorganization. Our measurement supports this interpretation. A single defect cannot cause a change of absorption that is as wide as illustrated in Fig. 4.18.

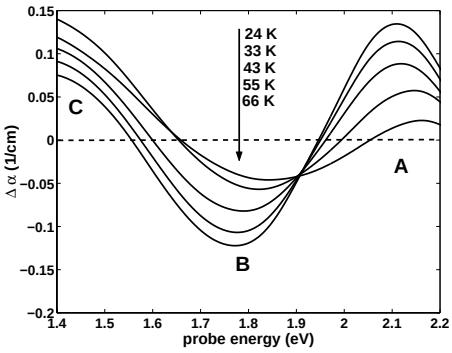

Figure 4.19: *For temperatures below 80 K we see a thermally induced charge transfer from one defect type absorbing at 1.8 eV (B) to another defect type absorbing at 2.1 eV (A). The existence of a point of constant $\Delta\alpha$ is an evidence that only two centers are involved. An isosbestic point means $\Delta\alpha = 0$: Probably because of an superimposed absorption band that does not change with temperature, this point of constant $\Delta\alpha$ is shifted downwards.*

During a cooling experiment, the same situation occurs in the opposite direction, the band gap is expanding, giving rise to absorption changes around 2.3 eV and at about 100 K a strong absorption is induced over the whole spectral range. In contrast to the heating experiment, the temperature induced charge transfer as shown in Fig. 4.19 is not seen. Apparently this observation requires exposure to light at low temperature. However, this observation remains unexplained.

The light induced metastability in $Sn_2P_2S_6$ is not only manifested in holographic sensitization [6] and persistent conductivity [27] but in a lasting change of absorption after exposure to band-band excitation.
At low temperature it is independent of the sample and dopants possible to partially redistribute the metastably trapped charges, whereas at room temperature those changes of absorption are difficult to detect: most probably this due to the high dark conductivity of $Sn_2P_2S_6$.

4.3 EPR

All attempts to detect EPR at room temperature failed (cf.section 3.2), so the following measurements all refer to temperature lower than 120 K.

4.3.1 X-Band

Without pre-illumination at either 295 K or 10 K there is no low temperature EPR at all. Taking into account the band gap shift to 2.5 eV at 10 K, green light (500 nm) will be transmitted at 10 K. In order to create effectively electron-hole pairs, we have to use light of at least 2.6 eV (470 nm).
EPR of a nominally pure sample is shown in Fig. 4.20. There are plenty of signals. The most intense lines are around 350 mT, corresponding to g-values close to that of the free electron.
Possibly several lines belong to a single defect state. To figure out which these are, we can refer to 1) the angular dependence 2) numerical simulation of the expected resonances 3) photo-EPR (see section 4.4). Signals that belong to a single defect state have necessarily the same spectral response.
In most cases measurements of angular dependence were carried out under permanent illumination with band-band-excitation, i.e. at 2.6 eV. Some centers, such as number 2 and 3, can be created by light of 1.5 eV and 2.0 eV respectively, as shown in Figs. 4.28 and 4.29; but they disappear within a few minutes after such illumination.
Here it has to be mentioned that EPR measurements of $Sn_2P_2S_6$:Fe failed. In this context it has to be considered that the high Fe-doping in this case (0.5 wt%, table 2.2) could have produced an impurity band leading to such a high conductivity that EPR observation is prevented. The EPR of Fe^{3+} could, however, be elucidated in crystals containing this ion as a background impurity. Selenium had no measurable influence on EPR. All subsequent results apply to $Sn_2P_2S_6$:Se (0.5 wt%) as well. The EPR of $Sn_2P_2S_6$:Se did not differ from undoped $Sn_2P_2S_6$.
Information on the g-tensors of centers 1 and 2, the range of g-values for centers 3 and 4 and the signal illustrated in Fig. 4.24 are given at the end of this section.

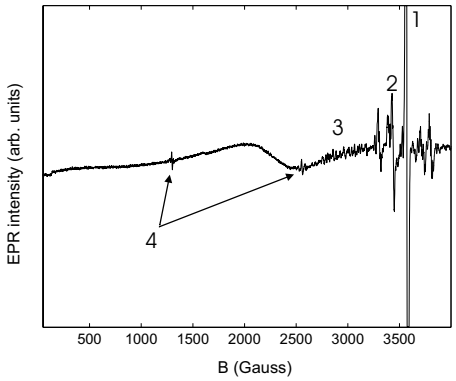

Figure 4.20: *EPR signals at 10 K in nominally pure $Sn_2P_2S_6$ under permanent illumination with 2.6 eV (470 nm). The wide signal around B=200 mT is shown in more detail in Fig. 4.24. Small lines around 300 mT, denoted 3, are signals and not noise.*

The angular dependence of these resonances for a rotation from $\vec{B} \parallel \vec{c}$ to $\vec{B} \parallel \vec{b}$ and to $\vec{B} \parallel -\vec{c}$ is presented in Fig. 4.21.

In Fig. 4.21 there are a lot of resonances between 220 mT and 360 mT belonging to centers 1,2 and 3. Figure 4.22 illustrates the angular dependence

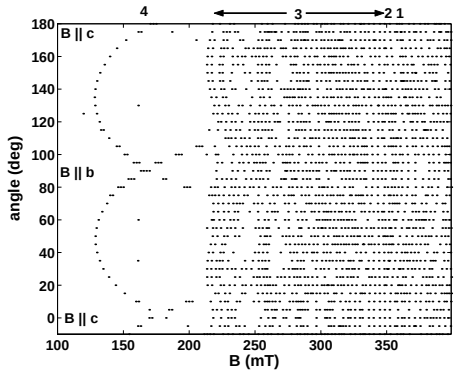

Figure 4.21: *EPR signals at 10 K in nominally pure sample 'New1'. The numbers correspond to those in Fig. 4.21.*

of centers 1 and 2 separately for rotation in one plane. The two resonances at higher magnetic field that are parallel to one of the crossing resonances, are discussed in section 4.3.1.

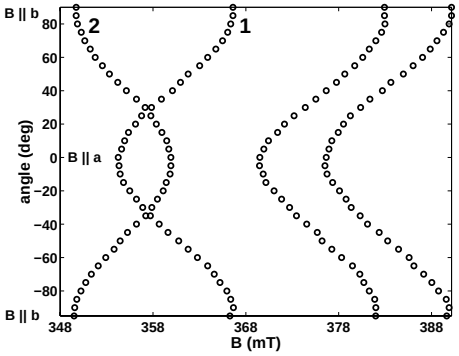

Figure 4.22: *Angular dependence of centers 1 and 2 for a rotation in the a,b-plane.*

In sample K3 the resonances of center 3 are smaller and only a few of them can be detected as shown in Fig. 4.23.

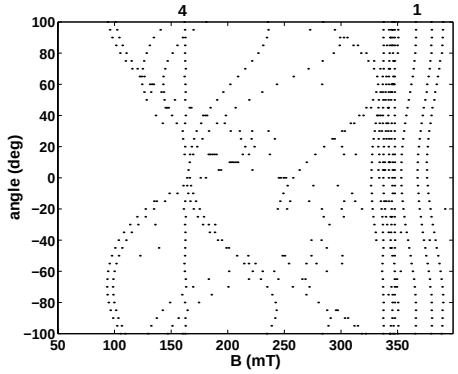

Figure 4.23: *EPR signals at 10 K in nominally pure K3 under permanent illumination with 2.6 eV (470 nm) light. There is an almost isotropic resonance at about 160 mT. Unfortunately the orientation of the investigated crystal fragment is unknown.*

Figure 4.23 illustrates that the presence of center 4 reduces the signal inten-

sity for center 3; this is a general observation in all samples where centers 3 and 4 where detected.
In only a single case an enormous signal, shown in Fig. 4.24, was observed. Although it could not be reproduced, this EPR is presented and discussed since it must have originated from the sample and was about two orders of magnitude larger than center 1.
This resonance occurred in a nominally pure sample K3 that had been exposed to band-band excitation at 295 K. The total signal intensity can be determined by numerical integration; it is at least two orders of magnitude larger than the other signals induced by blue light (2.6 eV) at 10 K. Since the signal intensity is proportional to the number of spins, it reflects the defect concentration. Unfortunately this signal could not be reproduced by any means: only one angular dependence is available therefore. With increasing temperature, the g-value of this resonance decreases (to about 2.0 at 120 K) but in contrast to all other signals reported above, this one was still detectable above 50 K.

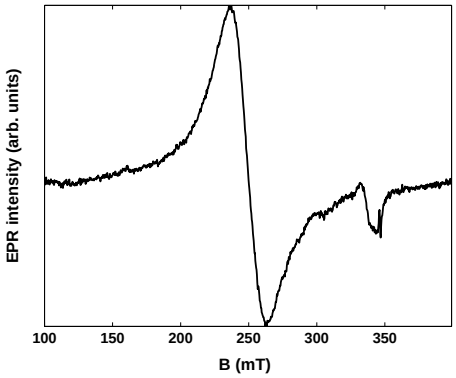

Figure 4.24: *Large EPR signal that occurred in a nominally pure sample K3 that had been previously exposed to band-band excitation at 295 K. The angular dependence of this signal is given in Fig. 4.25.*

The signal presented in Fig. 4.24 has an anisotropic angular dependence as shown in Fig. 4.25. This leaves no doubt that it is not an artifact but belongs to the sample.

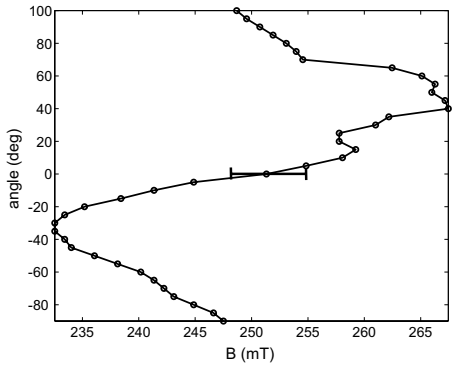

Figure 4.25: *Angular dependence of the large EPR signal in Fig. 4.24. The large errorbar arises from the slight asymmetry of the signal. This precludes an exact definition of the center of the signal. The angular dependence leaves no doubt that this signal belongs to the crystal.*

g-values

The angular dependence of EPR of centers 1 and 2 was taken from roadmaps for all three planes of rotation and numerically fitted to an effective $S = 1/2$ system. Center 3 denotes about a dozen of comparable resonances that can be assigned to a single defect type of center 3 (see Fig. 4.4). For center 4 such an investigation was not possible since it was impossible to detect the resonance in all three planes. So for centers 3 and 4 we give the range of observed g-values.

center	g-values
1	g_x=1.91715 , g_y=1.92360, g_z = 1.99505
2	g_x=1.94841 , g_y=1.99341, g_z = 2.01228
3	$\approx$ 2.1-3.29
4	$\approx$ 2.2-7.45

Table 4.2: g-values of centers 1 to 4

Superhyperfine interaction

Some of the EPR signals reveal a complex substructure that may only become visible in experiments with high resolution of the magnetic field. Fig. 4.26 and Fig. 4.27 show such hyperfine interaction. Depending on whether such splitting arises from the nucleus around which the wavefunction carrying the spin is localized or ligand ions, such splitting are called hyperfine or superhyperfine splitting.

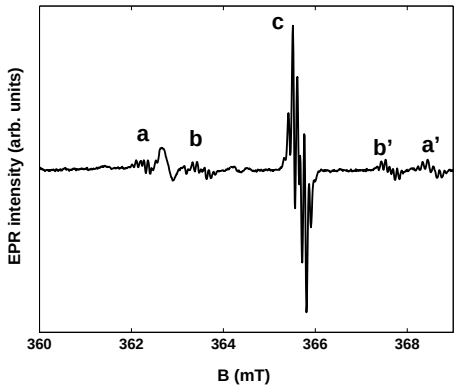

Figure 4.26: *Center 1: EPR signal under illumination with 2.6 eV (470 nm) light at 10 K. The groups a and b have analogues, a' and b', symmetric to c.*

Figure 4.26 shows a complex substructure of center 1. We see five groups of lines denoted *a, a*', *b, b*' and *c*. There are another two groups of lines *a*' and *b*' symmetric to group *c*. All these groups have the same angular dependence, their distances to line *c* are only extremely weakly depending on the orientation of the sample with respect to the magnetic field. Each of these five groups can be subdivided into single resonances. An expansion of the central group in Fig. 4.27 shows that 8 lines are partially overlapping. It is possible to separate these

resonances to obtain relative intensities. The components of the other groups *a* and *b* can not be separated easily. A closer look shows that groups *a* and *a*' are slightly wider that groups *b* and *b*'. We shall discuss this observation later.
The properties of center 2 are quite similar to those of center 1, as already indicated in table 4.3.1. Also one satellite line, running parallel to line 2 in Fig. 4.22 was observed, supporting the close relationship of centers 1 and 2. The fact that only one branch of satellite lines was observed in contrast to center 1, however emphasizes that the centers are different.

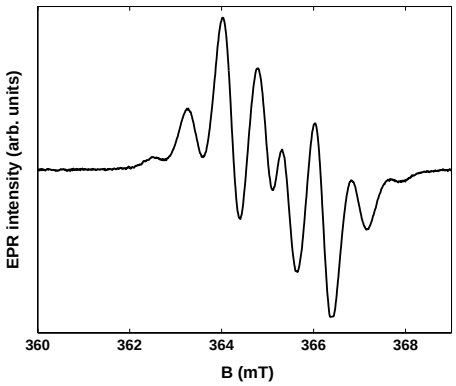

Figure 4.27: *Center 1 EPR signal under illumination with 2.6 eV at 10 K (see resonance c in Fig. 4.26). Modulation amplitude was 0.5 mT. Further increase of resolution yields no additional strucutre. Relative intensities of the separated resonances are 1:6:16:20:20:16:6:1.*

The central resonance, *c*, shown in Fig. 4.26 is shown in more detail in Fig. 4.27.

4.4 Photo-EPR

A parallel change of the intensities of optical absorption bands and EPR signals establishes a necessary condition for attributing them to the same microscopic origin. Without band-band excitation at low temperature the detection of EPR (including Photo-EPR) is impossible. Consequently all subsequent data refer to pre-illuminated samples.
In Fig. 4.28 the EPR intensities depending on pump energy for centers 1,2 and 3 is compared to the optical absorption changes at a probe energy of 1.5 eV in nominally pure $Sn_2P_2S_6$ as shown in Fig. 4.16.
The changes of EPR intensity shown in Fig. 4.28 and 4.29 show how spins, tied to their charge carriers, are transferred from one EPR center to another. The figures describe the situation after photoexcitation at 10 K. In Fig. 4.28 the black dashed line indicates that the change of optical absorption at $E_{probe} = 1.5$ eV is almost parallel to the change in EPR intensity for center 1 (red). For a pump energy of about 1.5 eV this EPR signal has disappeared, i.e. the respective defect state is depopulated. For the same pump energy another (green) EPR resonance rises: center 2. We can thus deduce that charge carriers are likely to be transferred from center 1 to center 2 by pump energies of about 1.5 eV.

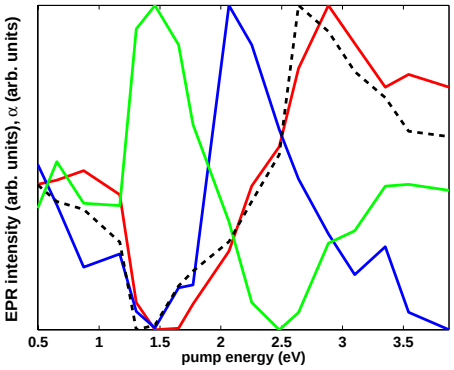

Figure 4.28: *After pre-illumination: Comparison of the light induced change of absorption (black, dashed) with EPR-intensities of center 1 (red), center 2(green) and center 3 (blue) depending on pump energy at 10 K. The change of optical absorption at 1.5 eV probe energy is almost parallel to the change of EPR intensity for center 1. At a pump energy of 1.5 eV the EPR of centers 1 and 2 are counter-propagating. Center 3 appears for excitation with 2.0 eV.*

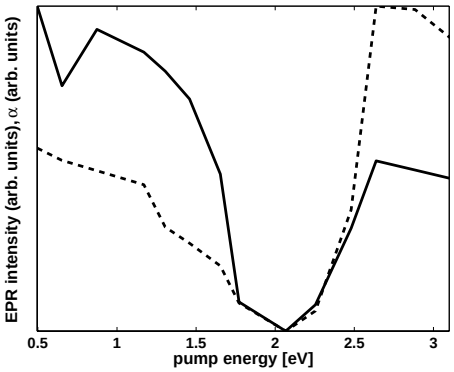

Figure 4.29: *Photo-EPR (solid) of center 4 compared to the change of optical absorption (dashed) at a probe energy of 2.0 eV in sample K3. This center is created under band-band-excitation at low temperature and diminishes in value for pump energies of about 2.0 eV.*

Center 2 is not stable under increasing pump energy. Above 1.6 eV its EPR disappears and only recovers under band-band excitation. At this pump energy of 2.0 eV two other EPR signals change as well. The EPR of center 3 (blue) rises while the EPR of center 4 also disappears (Fig. 4.29:solid). For pump energies exceeding the band gap, center 1,2 and 4 recover, while center 3 decays.
EPR shows that centers 1 and 2 are present in all samples under the previously described conditions. Comparison of centers 3 and 4 indicates that if center 4 is present, charges are more likely captured there than at center 3.

4.5 Photoconductivity

Before starting these measurements it is ascertained that the contacts show ohmic behavior. This is proven by Fig. 4.30 and shows that the contacts are properly applied and no silver paste is remaining on the other surfaces causing surface leakage. Depending on material and sample, transient currents have to decay. In $Sn_2P_2S_6$ 900 s are a typical time to wait until a steady state is reached

after changing light intensity or temperature.

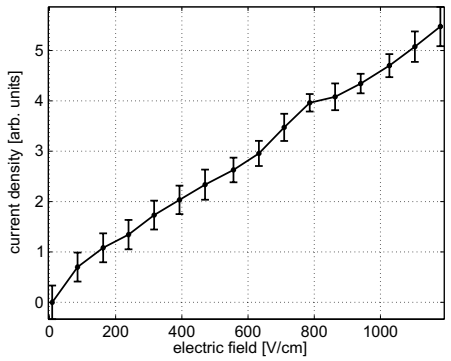

Figure 4.30: *Ohm's law is confirmed in a rectangularly cut nominally pure sample 'SPS 12' with silver paste electrodes at 295 K.*

The samples were illuminated with monochromatic light until a steady state of the photocurrent was reached. This steady state value was averaged over ten measurements.

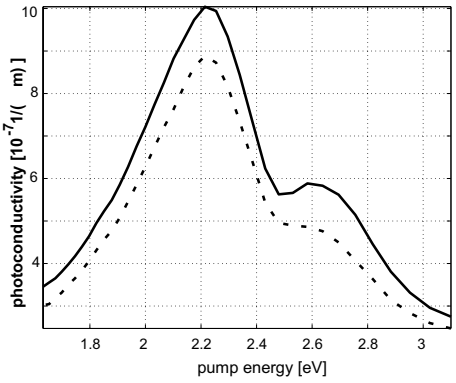

Figure 4.31: *Photoconductivity of nominally pure $Sn_2P_2S_6$ for two different voltages (200 V (solid) and 400 V (dashed)). Both curves show two maxima at about 2.2 eV and 2.6 eV.*

The data of photoconductivity presented in Fig. 4.31 are divided by the spectral intensity of each measurement to obtain the specific photoconductivity as illustrated in Fig. 4.32. Neither at 2.3 eV nor at 2.6 eV there are maxima of specific conductivity.

The curves published by Grabar [9] are qualitatively confirmed. Obviously the maximum of photoconductivity at 2.2 eV is an effect of the total available crossection.

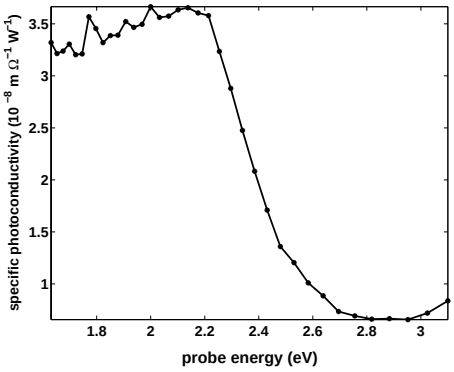

Figure 4.32: *Specific photoconductivity in nominally pure SPS 12. Typical intensities are* $\leq 50\ W\,m^{-2}$. *For energies exceeding the band gap the specific photoconductivity decreases exponentially within the experimental error.*

4.6 Pyroelectric luminescence (PEL)

Since the treatment of this subtopic has acquired quite high importance and a correspondingly large volume, a separate chapter, Ch. 6, is devoted to this field.

Chapter 5

Discussion

A general difficulty in assessing the experimental results obtained with $Sn_2P_2S_6$ is to distinguish between rules and exceptions. This is mainly due to the fact that crystals are difficult to grow and therefore limited in number. In addition to discriminating effects of the host lattice from those of defects, the light induced metastability is a further obstacle for the categorization of properties. Samples differ considerably in their properties depending on whether the metastable state has already relaxed or not.
Options for definite reference states are: a) a recently photosensitized sample and b) a sample that was annealed above T_C for several hours. For such a treatment Grabar [27] reports the loss of persistent conductivity, an indicator of the presence of a metastable excited crystal state.
Experimentally both preparations are problematic, the first since not all samples can be photosensitized, the second, since additional care has to be taken e.g. to prevent oxidation of the sample in air (see Appendix A.2).
In any case it is crucial to know what state of the sample the described data refer to.

5.1 Light induced charge transfer

Photoconductivity

Photo-excitation of charge carriers in an external electric field, leading to photoconductivity, is the most direct way to see light induced charge transfers. We reproduced the measurements of $\sigma_{\text{photo}}(E_{\text{pump}})$ by Grabar [27], however our interpretation is different.
The left maximum of the photoconductivity spectrum in Fig. 4.31 originates from the volume of the illuminated region in the sample in which photoconductivity exists. With increasing absorption coefficient α, the absorbing thickness is lowered to α^{-1}. This limits the photoconductivity for high absorption as indicated by the spectral dependence of the specific photoconductivity (Fig. 4.32). In that sense the left maximum in Fig. 4.31 cannot be attributed to a defect

level. This is furthermore supported by the increase of the peak position with decreasing temperature [27] caused by the shifting band gap.
For the photoconductivity maximum at pump energies of 2.3 eV-2.4 eV this consideration works just the other way round: If, due to the fundamental absorption, only a thin layer of estimated 50 μm [1], contributes to the photocurrent, the conducting sample volume decreases by about two orders of magnitude compared to the total bulk. In that respect the photocurrent we see arises from an extraordinary large concentration of carriers in a small volume.

Nevertheless such measurements cannot reveal the nature of the defect states from which carriers are excited. Such information can be obtained in favorable cases from EPR. On this basis we shall interpret the EPR-measurements and their combination with optical absorption spectroscopy. From this an overview on the detectable defect stats is derived. The subsequent sections will derive a light induced charge transfer model in $Sn_2P_2S_6$ starting from the identification of the involved defect states by means of EPR. We shall then interpret the light induced charge transfers between these defect states on the basis of photo-EPR data. This will assist in deducing a model for the charge transfer mechanisms of the photorefractive effect after light induced sensitization.

5.1.1 Identification of defect states

Let us start with the observation that without pre-illumination no EPR can be detected. This does not necessarily imply that all defects are diamagnetic; detection of EPR can be impeded by various mechanisms. But this observation proves that the defects are EPR-silent in their initial state.
Permanent illumination by band gap light at low temperature provides a vast density of both electrons and holes created by photoexcitation across the band gap. For sufficient intensities we can expect that existing defects can be rendered paramagnetic by capturing such holes or electrons. Such a situation might exist, however, only as an intermediate state in the sense of a dynamic equilibrium of capture and release of charge carriers.
EPR allows to figure out four main types of centers, denoted 1 to 4. By correlation with their optical absorption bands we could establish that these are involved in the dominant charge transfer processes of the investigated crystals. We shall discuss them now in detail.
It is helpful to know from the beginning whether the defects are involved in hole or electron transfer or even in both. From photo-electromotive force (photo-emf) measurements [8] and other holographic investigations [44] we know that the fast processes in holographic measurements in $Sn_2P_2S_6$ are caused by holes. We shall keep this in mind and see whether our considerations are consistent with the charge transfer of holes.
One main hint with respect to the interpretation of the observed EPR signals is as follows: Assuming a paramagnetic defect situated at a P site, this would always be neighbored by the other P ion of the P_2S_6 subunit. The defect-P

molecular orbital would have a high spin density at the P nucleus of the pair. To 100% it is ^{31}P with a nuclear spin of $I = 1/2$. A doublet hyperfine structure of the order of about 10 mT would be expected.
No spectra with such a definite signature are found. Thus paramagnetic defects substituting at a P site can be excluded. It is thus straightforward to discuss possible defects at the other sites.

Centers 1 and 2

Center 1 occurs in all samples no matter if they are intentionally doped or nominally pure. It can be created by band-band excitation at 10 K. The g-values of center 1 and center 2 (table 4.3.1) are close to the g-value of the free electron[1], g_e, and only weakly anisotropic. The ground state thus only has a small expectation value of orbital angular momentum, a condition fulfilled by an s-state. To such a state orbital character cannot be admixed in first order by spin-orbit coupling, because $\langle s|L_i|p\rangle$ is zero. The observed small difference to the g-value of the free electron can arise from higher order $\vec{L}\vec{S}$-coupling. This admixture depends on the relative orientation of the center's axes to the magnetic field, explaining the slightly different components of the g-tensor. If paramagnetism is caused by a shell that is less than half filled, the g-shift is usually negative, as found here.
Looking at possible candidates for an s-electron that is likely to occur in all $Sn_2P_2S_6$ samples, we find the $5s^1$ configuration resulting from a hole captured at a Sn^{2+} site. The initial Sn^{2+} is a $5s^2$ state that becomes $5s^1$ for Sn^{3+} with l=0, s=1/2.
We know that in ferroelectric $Sn_2P_2S_6$ Sn^{2+} occurs at two different sites. An unpaired electron located at such tin sites will have comparable g-tensors, since both are rather similar.
Often positive g-shifts are found for ions of (ns^1) type, increasing with the $\vec{L}\vec{S}$-coupling of the ligands and decreasing with the ligands' distances. In the ground state the hole is then partially delocalized to the ligands. The ligand shells are now almost completely filled, a situation characterized by positive g-shifts.
In the present case the Sn^{3+} is quite remote from the S-ligands [15]: we can therefore expect the described effect to be small. But as observed, the mean value for center 2 is slightly larger than for center 1. This is possibly due to the different environments of 7 respectively 8 neighboring S-ions. Since the positive g-value increases with the number of ligands we may conclude that Sn_1^{3+} (center 1) corresponds to the 7-fold coordinated site while Sn_2^{3+} (center 2) is correlated to the 8-fold coordinated site.
The subsequent discussion underlines that center 1 has a different environment than center 2 although for center 2 the outer lines (corresponding to *a,a'* in Fig. 4.26) were detectable as well. The inner lines analogous to *b* and *b'* (Fig. 4.26) could not be observed. This is probably due to the fact that white light is necessary to create center 2 and its superhyperfine satellites and white light

[1] mean g-value of center 1: 1.954, center 2: 1.984

creates numerous other resonances that are superimposed to these faint ones. The groups *a* and *b* in Fig. 4.26 are attributed to ligand (super-) hyperfine interaction with tin nuclei. It can be shown that the packet positions are different since they are caused by two tin ions at different positions relative to the central Sn^{3+} ion. Because the hyperfine splitting of the *a* packets, proportional to the distance from the central packet *c*, is larger than of *b*, the tin nucleus corresponding to *a* is closer to Sn^{3+} than that corresponding to *b*. The internal structure of each of these packets is due to additional hyperfine coupling with ^{31}P nuclei lying within the range of the Sn^{3+} wavefunction. This is proved by the similar structure of the central packet, *c*, which mirrors that of the outer ones, *a* and *b*. The central pattern arises from the same coupling to the ^{31}P nuclei, but the interaction with the tin nuclei is missing. Thus in the cases leading to *c* the unpaired electron visits only tin isotopes with $I = 0$.
The 4% difference of the nuclear moments of the magnetic (I=1/2) tin isotopes (^{117}Sn and ^{119}Sn) cannot be resolved in the spectra. The expected splittings are covered by the internal structure of packets *a* and *b*. Support for this interpretation is derived from the observation that packet *a* is somewhat wider than *b* (see Fig. 4.26). Since the hyperfine interaction with closer tin ions, leading to *a*, is larger, the nuclear moment difference between the isotopes is amplified correspondingly, leading to a larger packet width (Fig. 5.1). The present qualitative interpretation of the origin of packets *a* and *b* can be extended to a more quantitative level, accounting for the relative intensities of the outer packets as compared to the central one. These arguments are not given here. However, they support the presented model.

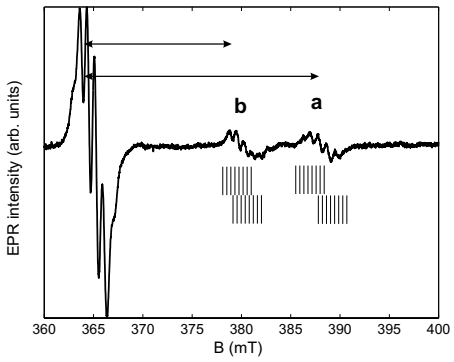

Figure 5.1: *Superhyperfine splitting (hfs) of the EPR of center 1 caused by two neighboring, inequivalent tin ions. Each of these packets contains contributions of the two magnetic tin nuclei. the influence of the 4% different nuclear moments is sketched exaggerated. The small splittings on all packets arise from phosphorus superhyperfine interaction.*

The ligand superhyperfine interactions of P and Sn, discussed above, can in principle be attributed to definite sites in the crystal with respect to the central Sn^{3+} ion. Such an assignment would necessitate, however, that the spatial dependence of the wavefunction of the unpaired electron could be calculated with high precision. The observed superhyperfine splittings essentially depend on the spin density at the respective sites. Because of the limited accuracy of such calculations no reliable conclusions can be made.
Not mentioned so far are the resonances expected for the cases where the Sn^{3+}

unpaired 5s electron interacts with its own magnetic nuclei (^{117}Sn and ^{119}Sn). Because of the expected corresponding high spin density the interactions would be tremendously strong, and simulations show that the corresponding resonances cannot be observed with EPR-measurements using frequencies around 9.8 GHz (X-band). Initial investigations at 34 GHz (Q-band) failed so far. Such measurements would have given the definite decision about the presented model.

Center 3

Most evident is that we see a large number of resonances with an identical dependence on pump energy as illustrated by the blue line in Fig. 4.28. The g-values of these obviously related defects and the angular anisotropy of their EPR signals indicate a pronounced contribution of angular orbital momentum, i.e. we observe a defect with $l \neq 0$, e.g. a p-electron. The most probable candidate for p-electrons occurring in many different positions is a hole captured at S^{2-} sites, creating S^{-}. Such an S^{-} is a $3p^5$ configuration, in other words a hole in an otherwise complete p-shell with $s = 1/2$ and $l = 1$.

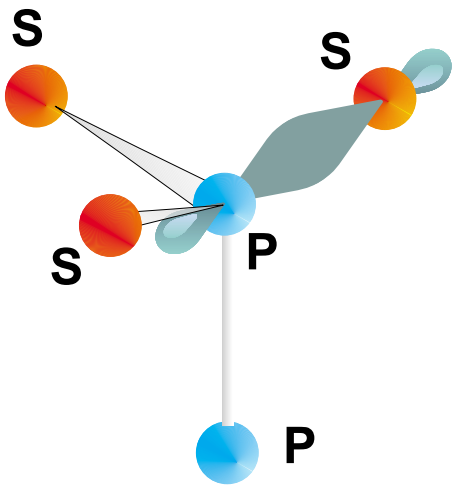

Figure 5.2: *Sketch of the sp-hybrid orbital in the binding of phosphorus and sulfur. A hole in this orbital will be repelled by the highly charged phosphorus. Therefore it will be located in the other sulfur orbitals pointing away from phosphorus. These are illustrated in Fig. 5.3.*

S^{2-} is mainly engaged in an sp-hybridized binding with P within the P_2S_6 subunit (Fig. 5.2). Interaction with neighboring Sn ions is weak, indicated by the large distances (0.27 nm to 0.35 nm [15]). A hole captured at an S^{-} site in the sp orbital will be repelled by the highly positive average charge of phosphorus, P^{4+}.

We assume therefore as a working model, that the hole is in those S^{-} orbitals that are pointing away from the phosphorus. These are all of p-type essentially. A possible sp-hybridization would be energetically favorable only if binding partners were nearby, stabilizing the the bond directions. However, the

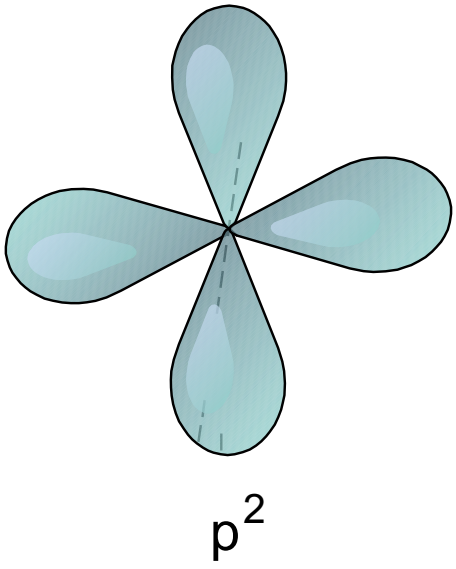

Figure 5.3: *Model for the S-orbitals containing the hole. The plane of the paper is perpendicular to the S-P-direction specified in Fig. 5.2.*

only conceivable bonding partners, the Sn^{2+} ions, are far away. Therefore it is reasonable to assume that we have to deal with two S^{2-} lone pairs (Fig. 5.3). A hole at S^{2-} can choose among these two. Within a P_2S_6 unit we can thus expect $6 \times 2 = 12$ possible orbitals for a trapped S^- hole.
Inside the unit cell we have two such P_2S_6 units: they are related by glide-mirror symmetry, but this symmetry operation does not transfer the orbital directions occupied by a hole into identical directions. Consequently we expect $2 \times 12 = 24$ equivalent directions of orbitals occupied by a hole. Each of these orbitals is characterized by S=1/2, leading to one magnetic transition between the corresponding substates ($m_s = \pm 1/2$) and thus to a single EPR-line. Their resonance fields are described by a Zeeman operator with an anisotropic g-tensor. Due to the low symmetry these resonances will only coincide by chance. We can therefore expect 24 lines, each of them possibly split by superhyperfine interaction with the neighboring phosphorus. These considerations show that the huge number of resonances attributed to center 3 in Fig. 4.21 is consistent with S^-.

Theory of EPR predicts that the difference of the observed g-values from the g-value of the free electron, g_e, is given by [38]:

$$\Delta g_{ii} \quad = \quad -2\lambda \sum_n \frac{|\langle 0|L_i|n\rangle|^2}{E_k - E_0} \tag{5.1}$$

Here $|0\rangle$ denotes the non-degenerate-p-ground state, $|n\rangle$ are the admixable excited p-states and the $\vec{L}\vec{S}$-coupling constant is denoted λ (about 330 cm^{-1} for S^-).
The smallest denominators are active when $\vec{B}$ is pointing along the S-P bond (see Fig. 5.2), i.e. perpendicular to the plane of Fig. 5.3. In that case the

relevant difference of energies is the one between the sketched p-orbitals (Fig. 5.3). They are almost degenerate. We can therefore expect large shifts away from g_e, and a maximum g of 3.3 is possible.
There will be slight splittings of the orbital energies, however, since the local S^- symmetry is not quite axial.

Center 4

The resonances summarized under this heading are characterized by a strong angular dependence of the resonance fields. For centers with S=1/2 this is not expected. Larger values of the spin are able to sample the surrounding crystal field by respective fine structure splittings resulting in considerable angular variations of the resonance fields.
In the present case the variations are typical of Fe^{3+} in lower than axial symmetry. The presence of Fe in nominally pure material is not surprising, since Fe is known to be one of the most frequent contaminations.
There is evidence that Fe is incorporated at least at two different sites in the lattice (see section 2.2.2). It is likely that all the angular dependent lines in Fig. 4.23 can be attributed to one type of Fe^{3+} centers. The observed isotropic g-value, 4.30 (Fig. 4.23), is highly typical of Fe^{3+} in a strong orthorhombic crystal field with a special ratio [45] of axial and orthorhombic compounds[2]. It will be shown that the observed Fe^{3+} centers result from Fe^{2+} by hole capture.

Two open questions remain: First, we have centers resulting from hole capture. Nevertheless electrons are excited as well and we have not yet commented on that. Second, the whole situation is metastable at 10 K and 295 K.

Electron centers

Since the EPR results do not give evidence for the fate of the electrons created by band gap illumination, we have to go back to more basic considerations to address this problem. It is known that such photoexcitation leads to persistent conductivity [27]. The trapped holes, on the other hand, can be reshuffled between different defects by light of energies below the band gap, as shown in Figs. 4.28, 4.29. The permanently conducting carriers are therefore likely to be electrons. The conduction band edge of $Sn_2P_2S_6$ has mainly $5p^1$ character (see Fig. 2.7 and Fig. 2.4). After photoexcitation the electrons thus will probably arrive in such states. An electron at a Sn site meets an ionically rather unstable situation, because Sn is only rather loosely bound among its S^{2-} neighbors. Therefore the lattice will distort around the capturing Sn ion, and the electron forms a polaron.

It should be possible to detect this particle by EPR, since $5p^1$ is paramagnetic. A further stabilization can occur if two such electrons distort the lattice

[2]Since it was not possible to follow all these center 4 resonances in three planes, neither the g-tensor nor the crystal field parameters could be determined.

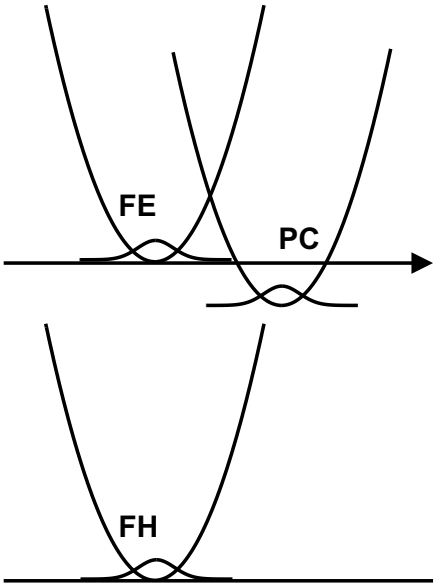

Figure 5.4: *Schematic illustration in configuration coordinate space of a situation leading to persistent conductivity, (PC). In this state, carriers (polarons or bipolarons) lead to strong distortion (large q) at each of the visited lattice sites. Recombination can only occur by thermal transition to the less distorted situation of the free electrons (FE). For strong distortion this is improbable because of weak vibronic overlap between PC and FE. Direct recombination with free holes (FH) is unlikely for the same reason.*

jointly by creation of diamagnetic bipolarons (see Fig. 5.4). This first explains that no EPR is observed, second it accounts for the extreme stability of the system of conduction electrons. Since bipolarons are much less mobile than polarons, this is also consistent with the tardiness of the electron gratings in photorefractive experiments with $Sn_2P_2S_6$[2].
Bipolarons can in principle be dissociated into single polarons [46], either thermally or optically. It is difficult, however, to realize the experimental conditions leading to dissociation without rapid recombination. It is possible that the huge resonance (Fig. 4.24), unfortunately observed only once, results from such a bipolaron dissociation. The properties of the EPR signal surely are pointing to the fact that it originates from the investigated $Sn_2P_2S_6$ crystal. The circumstances leading to its existence could not yet be reproduced and therefore no complete analysis can be given. It should be noted that Grabar [27] has attributed features of the dark conductivity to bipolarons. In that case, however, the crystal was not illuminated and was therefore in its groundstate with full valence and empty conduction band, and it is thus difficult to see how bipolarons could exist.

With these considerations we have derived a basis on which the photo-EPR measurements can be interpreted.

Photo-EPR

The effect of permanent illumination with white light on the sample is illustrated in Fig. 5.5.

As we see in Fig. 4.28 the situation immediately after photoexcitation is

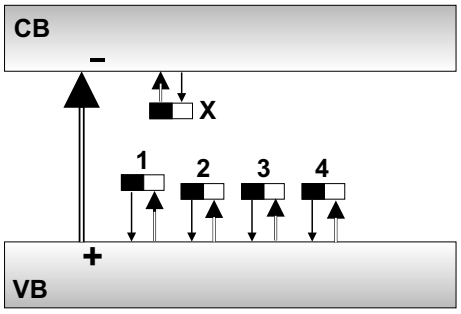

Figure 5.5: *Possible light induced charge transfer paths under permanent illumination with white light. The boxes comprise symbolically both optical and thermal charge transfer levels. Double arrows indicate primary processes, single arrows describe secondary processes. At this point we have no spectral information and cannot give energy levels relative to each other. Since every excitation energy* $\leq E_{gap}$ *is provided by the white light, all indicated charge transfer paths are possible. We will have to refine this picture on the basis of the photo-EPR data. VB denotes the valence band, CB the conduction band, while the numbers refer to the respective centers. The arrows always indicate the direction of the electron flow. Double arrows point to optical levels while single arrows start from thermal levels.*

as follows: For all centers, 1 to 4, there is detectable EPR intensity at low temperature. From Fig. 4.28 it is known that a pump energy of 1.5 eV (830 nm) transfers charges from center 1 to center 2, as indicated in Fig. 5.6.

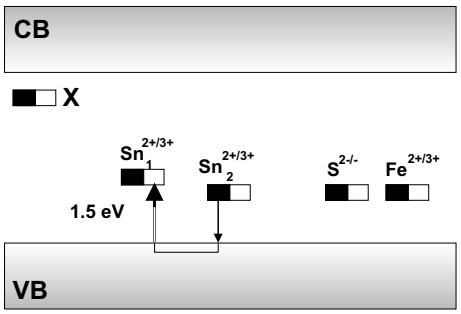

Figure 5.6: *Charge transfer corresponding to the change of EPR intensities shown in Fig. 4.28 at 1.5 eV pump energy. The EPR intensity of* Sn_1^{3+} *decreases while the EPR intensity of* Sn_2^{3+} *increases. This is explained by photoexcitation of an electron from the valence band to the* Sn_1^{3+} *defect state creating* Sn_1^{2+}*. The remaining hole in the valence band is combining with an electron from the* Sn_2^{2+} *state creating* Sn_2^{3+}*.*

We see that the $Sn_1^{2+/3+}$ state has to be deeper, since this is the initial state that was favorably created.
The situation for a pump energy of 2.0 eV (Figs. 4.28 4.29), is illustrated in Fig. 5.7. In terms of hole conduction, we see that holes are transferred from Fe^{3+} to sulfur, creating S^-. This explains the disappearance of the Fe^{3+} EPR, since EPR-silent Fe^{2+} is created and S^- resonances are rising.
One must keep in mind that all given defect levels are optical. As illustrated in Fig. 3.3, optical transitions occur into an excited state of a defect. Especially the maximum of the luminescence emission compared to optical absorption is

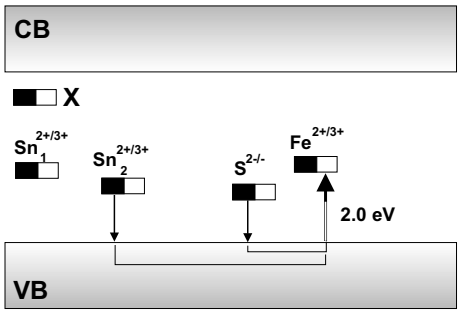

Figure 5.7: *Light induced charge transfer path for a pump energy of 2.0 eV as shown in figures 4.28,4.29. While the EPR of Fe^{3+} and Sn_2^{3+} diminishes in value the EPR of S^{-} rises, as we expect if holes are transferred from Fe^{3+} and Sn_2^{3+} to S^{2-} creating S^{-}.*

Stokes-shifted towards lower energies by the difference of optical and thermal level.

5.1.2 Hopping conductivity versus band conductivity

For most oxide materials the band transport model came out to be the most efficient description of transport mechanisms in holographic experiments [10]. In order to explain, why light of 1060 nm used for infrared recording in photoexcited $Sn_2P_2S_6$ does not decrease the number of traps, a model for hopping conductivity was suggested [34]. In putting forward this argument it was assumed that photoexcitation of a charge carrier from traps - in the present case: holes to the valence band - would lead to recombination with electrons in the conduction band. This does not necessarily occur under the conditions of persistent conductivity. In this situation the electron state has very little vibronic overlap with the holes and recombination is thus unlikely (Fig. 5.4). In addition to that, it has to be considered that hopping requires overlapping wavefunctions of the initial and the final defect state. It is unlikely that light generates sufficiently large defect concentrations that this condition can be fulfilled. In other words: for hopping conductivity we have to postulate about one photoinduced defect per unit-cell. In such a case much larger changes of various crystal parameters such as persistent conductivity, optical absorption etc. are expected.

5.2 Relevance for the holographic properties

The present investigation has shown that sensitization of $Sn_2P_2S_6$ by white light illumination, corresponding to band-band excitation, leads to the formation of two subsystems, electrons and holes, which are stabilized against recombination with each other. The stabilization is probably caused by the extraordinarily strong lattice relaxation induced by the electron subsystem. This is supported by the observation of persistent conductivity, indicating that the lattice is distorted around the electrons hopping between equivalent conduction band lattice sites, to such an extent that recombination with holes becomes unlikely because of small vibronic overlap (Fig. 5.4).

In a sensitized crystal holograms are written with light of energies below the band gap. This is supposedly caused by reshuffling the holes among the traps identified in this investigation. One can think of transfers corresponding to the one-center model [10], where only one type of defect is involved, possibly the primary Sn^{3+}. This absorbs at 1.5 eV (830 nm) at low and at 1.3 eV (950 nm) at room temperature. Alternatively, more than one defect might be involved, according to the two-center model [10]. The absorption of Fe^{3+} might be utilized in this manner: it absorbs at 2.0 eV (620 nm) at 10 K and at 1.8 eV (690 nm) at 295 K.

It was observed that the fast hole gratings are slowly compensated by other carriers [2]. These are certainly electrons, having a low mobility because of their strong coupling to the lattice.

A special property of $Sn_2P_2S_6$ is its high room temperature photorefractivity at 1064 nm. This can be caused by the low energy wings of the Sn^{3+} absorption band, peaked at 1.3 eV (950 nm) at 295 K. Other defects cannot be excluded, however. Further studies, utilizing future OMA spectrometers extending to longer wavelengths, could show whether there are separate absorption bands at low energies.

No statement can be made with respect to the unintended defects in 'dark'. $Sn_2P_2S_6$, sensitizing the material without preillumination.

Chapter 6

Pyroelectric luminescence

6.1 Introduction

In 1969 Schmidt and Petersson [47] reported 'electric sparks' in ferroelectric triglycine sulfate (TGS). Six years later, Yockey and Aseltine [48] wrote about 'high voltage discharges' after γ-irradiation of other ferroelectrics like Rochelle salt, guanidinium aluminium sulfate hexahydrate (GASH) and potassium dihydrogen phosphate (KDP) under temperature ramps. It soon came out that irradiation with γ-rays is not a necessary precondition for the observation of discharges since it was only one year later that Cooke and Alexander [49] emphasized the 'unirradiated' state of glycine that also exhibited 'scintillations'. Later several other publications followed reporting this type of luminescence in tourmaline [50], $LiNbO_3$ [51, 52], proustite and pyrargyrite [53], sodium nitrite and ammonium tartrate [54], N-isopropylcarbazole [55] and various other materials [56].

The term 'pyroelectric luminescence' (PEL) was coined by Patel and Hanson [56] in 1981 for two radically different observations. First, the spike-like discharges through the ambient atmosphere (see Fig. 6.1, Fig. 6.2) and second, a smooth emission slowly varying with temperature and consequently with time. For brevity we shall refer to this smooth pyroelectric luminescence as SPEL.
The spike-like discharges and their dependence on ambient gas, atmosphere pressure and heating rate have been clarified conclusively by Dreger and Kalinowski [57]: All ferroelectrics show a change of polarization under changing

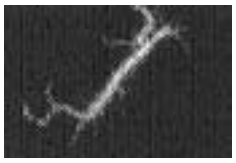

Figure 6.1: *A flash occurring from a KDP sample under temperature change [48].*

temperature that defines a pyroelectric coefficient γ_{p}:

$$\gamma_{\mathrm{p}} = \frac{dP}{dT} \tag{6.1}$$

$$P = \int_{T_0}^{T} \gamma_{\mathrm{p}}(T)dT \tag{6.2}$$

$$= \int_{0}^{t_{end}} \gamma_{\mathrm{p}}(T)\beta dt \tag{6.3}$$

Here β denotes the constant heating rate. Equation 6.2 only holds for 1) idealized materials with zero dark conductivity and 2) perfectly insulating ambient gas. If not, both contributions will partially compensate the polarization. We shall pay more attention to that in the next paragraph. Since all measurements were carried out in He atmosphere, we neglect the contribution of adsorbed ions on the sample surfaces.
This polarization corresponds to a macroscopic internal electric field that is identical to the electric field along the outer edges of the specimen:

$$E = -\frac{P}{\epsilon_0} \tag{6.4}$$

For a detailed argumentation refer to [58, 59] and Appendix B. The small dark conductivity at low temperature causes electric breakdown through the ambient atmosphere that regularly resets the electric field.

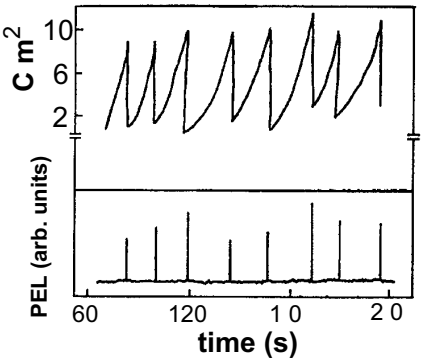

Figure 6.2: *Surface charge density Σ on a N-isopropylcarbazole crystal under decreasing temperature (top) and spike-like emission through the ambient gas (bottom) as reported in [57]. Gas pressure was $5{\cdot}10^4$ Pa and the maximal surface charge density corresponds to about 1 MV/m.*

6.2 Experimental results

The results presented in this section are obtained with sample K3, freely mounted during the measurements. Since the PEL properties of $Sn_2P_2S_6$, including

smooth pyroelectric luminescence (SPEL),are similar to those of other pyroelectrics, the present studies can be considered to be paradigmatic for other pyroelectrics exhibiting such phenomena.
Only below about 190 K the material exhibits discharge bursts during cooling and heating. The SPEL (Fig. 6.3) is not accompanied by spikes and occurs during heating above 190 K, if the crystal had been exposed to band-band (2.3 eV) illumination at 295 K, i.e. at a temperature higher than the SPEL maximum, before cooling to 4.2 K in helium atmosphere. Because of the low intensity of the emitted light, the luminescence could not be resolved spectrally. Without further exposure to light, the emission intensity remains almost unchanged in the same temperature range from 190 K to 230 K throughout at least ten cooling and heating runs.

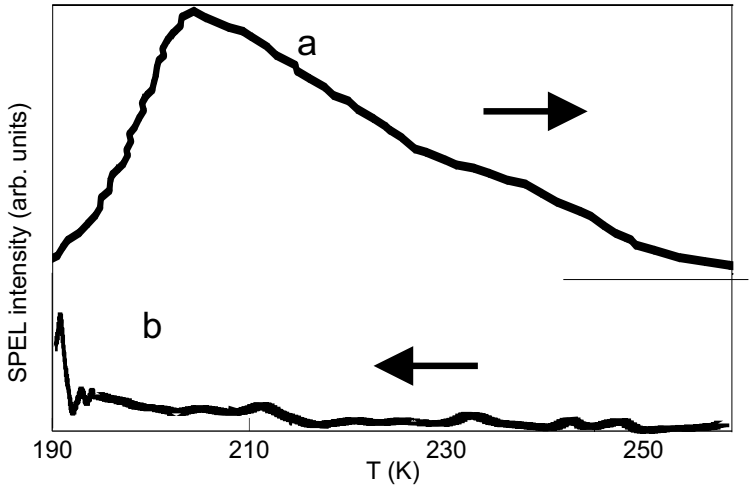

Figure 6.3: *Pyroelectric luminescence for heating (a) and cooling (b) in nominally pure $Sn_2P_2S_6$ sample K3 after photoexcitation at 295 K. Because of the low intensity of the emitted light, the luminescence could not be resolved spectrally. For clarity the zero level of a has been shifted upwards, as indicated.*

In this context it is worth noticing that the material shows persistent conductivity [27] after band-band photoexcitation at 295 K. This conductivity, pointing to a pronounced metastability of the photoinduced excited state of the crystal, remains essentially unabated during all the described heating and cooling cycles. Only after storage of a sample in the dark for several weeks SPEL diminishes in intensity and can then be observed merely during one heating run. If the heating is stopped during the emission process, SPEL decays quickly. Also an external short-circuit of the crystal suppresses SPEL.
Especially the last two observations underline that SPEL is based on the release of trapped charge carriers triggered by the pyroelectric field: no luminescence

occurs if the field is short-circuited, either internally by the dark conductivity σ_D or externally. This is further supported by the absence of the effect in centric compounds, such as $SrTiO_3$, whereas it occurs in closely related acentric materials, such as $BaTiO_3$.

6.3 Discussion

Despite of similarities of this SPEL to usual thermally stimulated luminescence (TSL), several observations do not meet this comparison:

1. SPEL occurs without previous low temperature photo-excitation
2. traps are not completely exhausted by exceeding the temperature at which SPEL is observed
3. analysis of SPEL, using established methods for TSL, yields unreasonable values for the trap depths, sometimes even temperature dependent [52]
4. in some materials SPEL also occurs under cooling [53]
5. if the temperature rise is stopped, the luminescence rapidly ceases

The results listed above underline that SPEL is based on the release of trapped charge carriers triggered by the pyroelectric field: no luminescence occurs if the field is short-circuited, either internally by dark conductivity σ_D or externally.

6.4 Poole-Frenkel effect in a pyroelectric

It is thus straightforward to invoke the Poole-Frenkel-effect [60] to explain the SPEL (Fig. 6.4): The pyroelectric field at the site of a trapped charge carrier can lower the escape barrier to such an extent that recombination, accompanied by luminescence, takes place. In the absence of the pyroelectric field the barrier is high enough to prevent detectable emission.

Therefore it is necessary to discuss the conditions under which the pyroelectric field can develop fully. At low temperatures it is short-circuited within more or less regularly spaced time intervals by the spike-like external discharges. The pyroelectric field is furthermore counteracted by the dark conductivity σ_D increasing with temperature (Fig. 6.6). SPEL is thus essentially observed only in the temperature window bracketed by discharges at low temperature and excessive conductivity at high temperature.

These points are now elaborated quantitatively: For a Coulomb-like potential of barrier height W_A, lowered by W_{PF} via the Poole-Frenkel effect, the

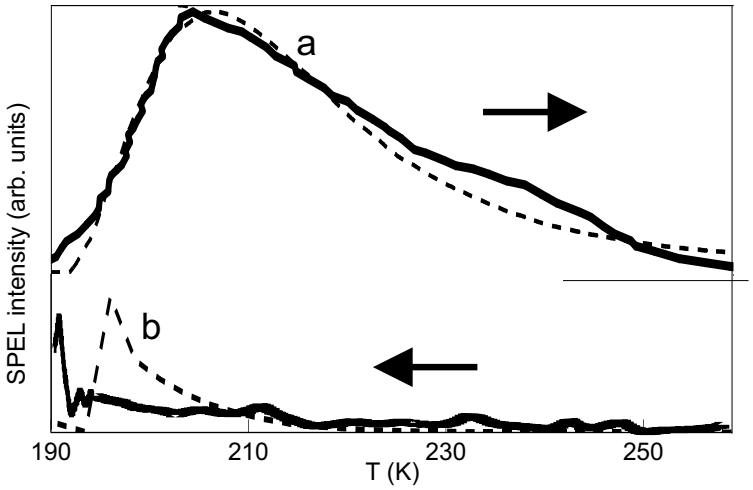

Figure 6.4: *Temperature dependence of the smooth PEL of $Sn_2P_2S_6$ measured (solid) and simulated (dashed) under heating (a) and cooling (b). For clarity the zero level of (a) has been shifted upwards.*

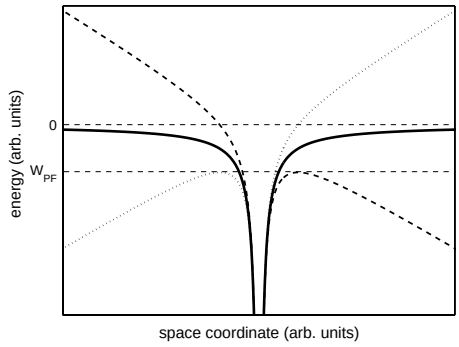

Figure 6.5: *Poole-Frenkel lowering, W_{PF}, of a Coulomb escape barrier (solid) for two pyroelectric fields of opposite polarity, occurring during heating or cooling of a pyroelectric.*

probability that a trapped charge carrier is thermally excited to the effective barrier height is given by:

$$\frac{N}{N_0} = \exp\left(\frac{-(W_{\mathrm{A}} - W_{\mathrm{PF}})}{kT}\right) \tag{6.5}$$

, where N_0 is the total number of captured charge carriers. The fact that repetitive heating, even to temperatures above the maximum of SPEL, does not significantly decrease the number of such carriers allows to neglect the temperature dependence determined by W_{A}. The macroscopic pyroelectric field inside the crystal, leading to W_{PF}, is given by $E_{\mathrm{P}} = -P/\epsilon_0$, where P is the pyroelectric polarization. Note that this field does not depend on the relative dielectric constant [58, 59]. W_{PF} is calculated as follows: The potential U of a carrier,

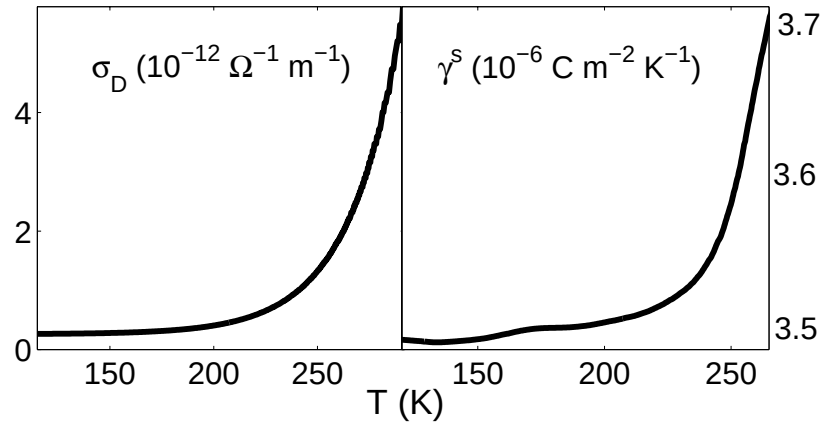

Figure 6.6: *Temperature dependence of the dark conductivity $\sigma_{\rm D}$ [10] and the pyroelectric coefficient $\gamma^{\rm s}$ [14] of $Sn_2P_2S_6$.*

trapped in a Coulomb well and additionally exposed to $E_{\rm P}$, is

$$U = eE_{\rm P}r + \frac{e^2}{4\pi\epsilon_0 r} \tag{6.6}$$

The resulting barrier lowering is:

$$W_{\rm PF} = \sqrt{\frac{e^3 P}{\pi\epsilon_0^2}} \tag{6.7}$$

By comparison with Eq. 6.5:

$$\frac{N}{N_0} = \exp\left(-\frac{W_{\rm A}}{kT}\right)\exp\left(\frac{\sqrt{\frac{e^3P}{\pi\epsilon_0^2}}}{kT}\right) \tag{6.8}$$

The developing pyroelectric polarization P is determined by two opposing influences (Eq. 6.9): a build-up, given by the heating rate β and the pyroelectric coefficient $\gamma^{\rm s}$, and its relaxation, described by the Maxwell time $\tau_{\rm M}(T) = \epsilon_0/\sigma_{\rm D}(T)$. Note that also here the relative dielectric constant does not appear. Since the sample was mounted freely in the experiment, the unclamped, secondary pyroelectric coefficient $\gamma^{\rm s}$ appears in Eq. 6.9:

$$\frac{dP}{dt} = \gamma^{\rm s}(t)\beta - \frac{P\sigma_{\rm D}(t)}{\epsilon_0} \tag{6.9}$$

Using the temperature dependent values for $\gamma^{\rm s}$ [24] and $\sigma_{\rm D}$ [27], as shown in Fig. 6.6, as well as the heating rate in the experiment ($\beta = 1.5 \cdot 10^{-1}$ K/s) we arrive at the dashed curves in Fig. 6.4 by numerical integration of Eq. 6.9.

Here $P(t)$, resulting from this procedure, was translated into the corresponding temperature dependence $P(T)$, taking account of the constant heating rate β. Inserting $P(T)$ into Eq. 6.8 and setting N proportional to the emission intensity, it is seen (Fig. 6.4) that the experimental data are well reproduced. This does not only concern the temperature dependence of SPEL for heating, but also the almost complete vanishing of SPEL under cooling (Fig. 6.4(b)) is described adequately as well. At first sight, the dissimilarity of SPEL under heating and cooling is astonishing since P should equally develop in both cases. Because of the integration process, however, $P(T)$ is not determined solely by the current values of $\gamma^{\mathrm{s}}(T)$ and $\sigma_{\mathrm{D}}(T)$ but also by their development in the past. The high SPEL during heating is essentially caused by the low σ_{D} at the initial temperatures, whereas cooling collects the influences of the rather high σ_{D} at elevated temperatures, i.e. a permanently suppressed E_{P}.
For heating, the integration of Eq. 6.9 was started at 190 K, taking into account that the last spike in this experiment occurred near this temperature. Apparently only above 190 K the conductivity σ_{D} is high enough to prevent that the pyroelectric field E_{P} reaches the breakdown threshold of an estimate value of 6 MV/m [61]. The initial temperature for the cooling integration was taken to be 290 K. Here P was set to zero, and the absolute values of P resulting from integration towards lower temperature were inserted into Eq. 6.8. Since the integration extends into regions of low σ_{D}, here the discharge threshold of E_{P} was reached near 190 K. This is seen from Fig. 6.4(b), where both simulation and experiment indicate discontinuous changes of the PEL, attributed to discharge. Also an increase of SPEL towards lower temperature is evident in both curves of Fig. 6.4(b). In all these features the asymmetry between heating and cooling which has been discussed before is evident.
The lowering of the barrier, W_{PF}, and the values of the pyroelectric field for heating and cooling are shown in Fig. 6.7. An initial barrier height, W_{A}, of 0.3 eV was assumed. The change of activation energy by W_{PF} is considerable.

Moreover the model predicts a rapid decay of the luminescence after the heating is discontinued at a temperature T_0.

6.4.1 Time evolution of SPEL intensity

The unexpected rapid decay of the pyroluminescence signal for fractional glow measurements is predicted by the model of the pyroelectrically induced Poole-Frenkel-effect. If we assume that heating is discontinued at an arbitrary point of time T_0 during the occurrence of SPEL, we arrive at the following equation:

$$\frac{N(t)}{N_0} = \exp\left(\frac{-W_{\mathrm{A}}}{kT}\right) \cdot \exp\left(\frac{\sqrt{\frac{e^3 P_0}{\pi \epsilon_0^2} \exp\left(-\frac{t\sigma_{\mathrm{D},0}}{\epsilon_0}\right)}}{kT}\right) \tag{6.10}$$

This expression takes into account that the pyroelectric field, $E_{\mathrm{P}}(T_0)$, is short-circuited within the Maxwell time, $\tau_{\mathrm{M}}(T_0) = \sigma_{\mathrm{D}}(T_0)/\epsilon_0$. For $T_0 = 200\ K$,

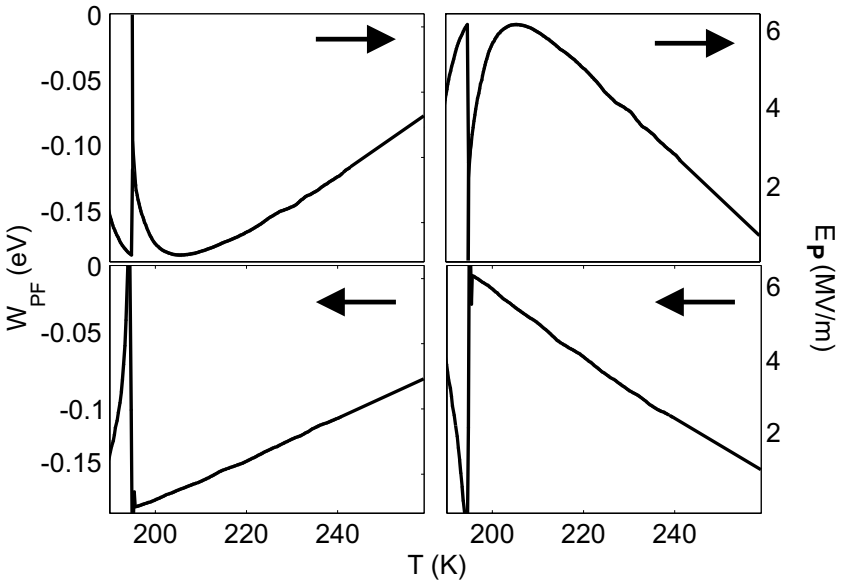

Figure 6.7: *Temperature dependence of W_{PF} and E_{P} during heating and cooling derived from the data in Fig.3. Integration for heating started at 180 K with an initial value $P = 0$. Discharge threshold was taken to be 6 MV/cm, leading to $W_{\mathrm{PF}} = 0$ and $E_{\mathrm{P}} = 0$ at about 190 K. Cooling integration started at 290 K.*

$\tau_{\mathrm{M}} = 15$ s. The decay time derived from Eq.6 is significantly shorter ($\tau_{1/2} \approx 2$ s) because τ_{M} enters in the exponent. Experimentally the decay time was found to be less than 10 s. Only an upper limit can be quoted, because due to the faintness of the SPEL signal the experiment had to be operated with an integration time of 10 s and could therefore not resolve shorter times.

6.4.2 Pyroluminescence and phase transition

In section 6.2 we have seen that the predominance of γ^{s} or σ_{D} determines the occurrence of spike-like or smooth pyroelectric luminescence. The probability to observe SPEL in the vicinity of a phase transition, where γ^{s} is large, is therefore drastically increased.

6.4.3 Piezoluminescence

It is only a consequence of what is deduced above: the origin of the field that triggers the Poole-Frenkel-effect is not necessarily the pyroelectric field but can be an external field or the piezoelectric field. In other materials the latter one can be large enough to cause these spikes [62]. It depends on the speed of pressure change if either discharge bursts (rapid change) or SPEL (rather

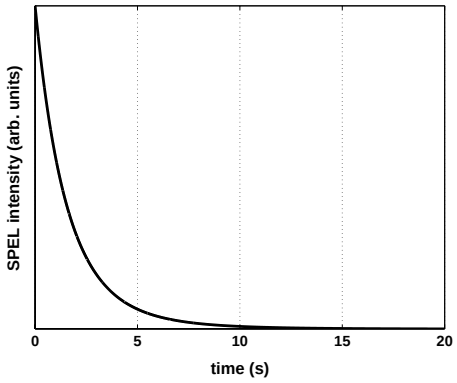

Figure 6.8: *Temporal decay of the SPEL signal. The integrated intensity of the first 10 s, corresponding to the experimental resolution, is more than 60 times larger than of the second 10 s. This decay is not simply exponential.*

slow change) predominate, but there is no doubt that the piezoelectric tensor elements in $Sn_2P_2S_6$ are sufficiently large to cause an electric breakdown and consequently the smooth luminescence as well.

We have presented a model that explains the essential features of the SPEL in $Sn_2P_2S_6$ under the assumption that the pyroelectric field enables the release of trapped charge carriers by lowering the barrier via the Poole-Frenkel-effect. There are indications that this interpretation, based on the experimental data of $Sn_2P_2S_6$, is representative for the luminescence behavior of pyroelectrics universally. In contrast to TSL, in SPEL the barrier height is not fixed but changes under the pyroelectric field. This introduces an additional temperature dependence. The model accounts for the difference of SPEL under heating and cooling, the limited temperature range of SPEL, the stability of the light-induced crystal state above the temperature of SPEL, the sudden stop of SPEL when heating is discontinued and the impossibility to determine trap depths by conventional TSL methods.

Chapter 7

Conclusion

$Sn_2P_2S_6$ has demonstrated its potential in various holographic measurements. Since further advances in the understanding and optimization of this material depend on the identification of its defect structure, the presented investigations were carried out. Combined EPR-optical absorption spectroscopy helped to unravel the most prominent defect states and to figure out the light induced charge transfer paths.
Initial band gap illumination establishes a metastabely excited crystal state creating persistent conductivity, a large photorefractive gain and, as we could show, a lasting change of absorption. These phenomena are interpreted in terms of the consequences of electron and hole formation by band-band illumination.
The behavior of the photogenerated holes at 10 K is followed by EPR and simultaneous EPR-optical absorption spectroscopy. Sn_1^{2+} captures a hole at one tin site forming Sn_1^{3+}. In the same way Fe^{2+}, most likely incorporated on tin sites, captures a hole forming Fe^{3+}.
Additional illumination with light of 1.5 eV (830 nm) transfers the holes from the first tin site Sn_1^{3+} to the second one, forming Sn_2^{3+}. This situation is rather unstable since further increase of excitation energy to 2.0 eV (620 nm) moves these holes from Sn_2^{3+} away to S^{2-}, becoming S^-. At the same time and more evident for excitation with 2.0 eV is the light induced charge transfer from Fe^{3+} to S^{2-}, creating S^-.
These considerations are consistent with the experimental observation of holes as the fast charge carriers after photosensitization. On this basis and additional EPR investigations we elaborated a model that attributes the persistent conductivity and consequently the metastabely excited crystal state to the formation of electron bipolarons on Sn sites.
Optical absorption studies perfectly confirmed the expanding band gap for decreasing temperature. This is qualitatively used to reconsider the interpretation of former photoconductivity measurements. The absorption bands are demonstrated to have widths comparable to those in oxides.

The puzzling phenomena observed during the attempt to study thermally

stimulated luminescence in pyroelectrics have given this field a separate label: pyroelectric luminescence (PEL). Its main features had not been understood for about 20 years. Using the PEL properties of $Sn_2P_2S_6$ as a paradigm for the whole class of pyroelectrics, a model is developed to explain the main features of the effect: charge carriers are released by a Poole-Frenkel lowering of the trap barrier induced by the pyroelectric field under changing temperature.
The model is able to reproduce the temperature dependence of PEL for heating and cooling as well as its time dependence, using a single set of experimentally determined parameters.

Appendix A

Growth

A.1 Phase diagram

The phase diagram given in Fig. A.1 indicates a peculiarity of $Sn_2P_2S_6$.

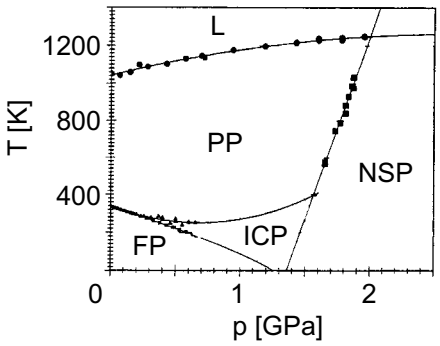

Figure A.1: *Phase diagram of $Sn_2P_2S_6$ as published by Tyagur and Yun [63]. 'L' denotes liquid, 'PP' paraelectric phase, 'FP' ferroelectric phase, 'ICP' incommensurate phase and 'NSP' new solid phase. These phases are discussed in detail in [63].*

Along the temperature scale at zero pressure, a displacive second order phase transition from the ferroelectric to a paraelectric phase occurs at T_C=339 K[1]. The melting point is at 1050 K.
A *tricritical point* exists where the ferroelectric phase, the paraelectric phase and the incommensurate phase meet. This is at a value of T=337 K and p=0.17 GPa [64]. A *Lifshitz point* is defined as a point separating the high temperature disordered phase and the low-temperature commensurate and incommensurate phase. In the conventional definition the transition to the low-temperature phases are considered to be continuous. In $Sn_2P_2S_6$ the term 'tricritical Lifshitz point' is used to express that these points coincide. This point was subject to intense investigation of critical phenomena in thermodynamics [64, 65, 66].

[1]The value of the phase transition temperature varies between 337 K and 341 K.

A.2 Methods

Metal-phosphorus-sulfur ($Me_xP_yS_z$) compounds are not new. At the end of the nineteenth century they were grown by reaction of MeCl with e.g. P_4S_{10} [67]. Sometimes even elementary synthesis was employed [68, 69]. In the 1960s, the compounds of $Me_2^{II}P_2S_6$ type had a renaissance. The metals investigated so far are Fe, Sn and Pb. Sulfur can be easily replaced by selenium.
Several methods to grow $Sn_2P_2S_6$ are known and reported in literature. For the mentioned optical applications it is vital to have *sufficiently large* and *optically perfect* samples that can be *doped voluntarily* and that avoid undesirable pollution that will result in scattering and other undesirable properties.

Vapor transport growth

Special care is taken with sulfur, that is cleaned in several subsequent recrystallizations [19]. Tin has less than 0.001% contamination that is mainly different metals without predominance [19]. Amounts of the components far from stoichiometry and a transport gas (typically iodine) are given into an evacuated quartz tube. It is worth mentioning that the transport gas itself has strong influence on the properties [9]. If the commonly used SnI_4 is replaced by SnI_2 the samples have an additional absorption band (see chapter 4.1). Even contamination with silicon from the quartz tubes is discussed [70]. The iron-doped material was grown by I.M. Stoika [19].
The tube is closed and annealed to 650° C to 700° C. At this temperature the elements last for about 4 h to react. Then the tube is brought into a temperature gradient, where the transport occurs by convection. The crystallization takes place at the cold end of the tube. A typical transport rate is in the order of 50 mg h^{-1}, i.e. several days of growth for reasonably large samples.
There are also samples grown by the Bridgman-Stockbarger method but often they suffer from insufficient optical quality and evident cracks.

Room temperature synthesis

A major drawback of the previously described growth mechanisms is the comparably slow growth rate of only about 50 mg/h. That is an evident limitation for industrial application. But not all applications require bulks (cf. section A.2) and in 1997 X. Bourdon et al. [71] published a way to synthesize nanoparticles at room temperature. The following chemical reaction takes place in aqueous solution.

$$2SnCl_2 + Li_4P_2S_6 \rightarrow Sn_2P_2S_6 + 4LiCl \tag{A.1}$$

It is decisive to double the ratio of Sn to P that is requested by stoichiometry to suppress the growth of $Sn_1P_2S_6$. Investigation of the nanocrystallites showed unambiguously the monoclinic structure of $Sn_2P_2S_6$ although the authors do not explain which one. The size of the nanocrystallites is estimated to be less

than 20 nm, a size that does not allow ferroelectricity to build up since surface contributions dominate. And it is possible that polarization fluctuation are on a length scale that is comparable to the particle dimension. The critical particle size was estimated as 20 nm $\leq$ d $\leq$ 76 nm.
It is now challenging to use this method to grow larger samples and to avoid the presence of chlorine that is always incorporated up to 1% so that it is not longer a defect but mixed crystals.
It is worth mentioning that for $Sn_2P_2Se_6$ the growth of nanoscopic single crystals in a photopolymeric host succeeded [72]. Almost all bulk properties accessible with nanoparticles were confirmed. For some applications such as films or ceramics this is an alternative approach.

Films

The first successful growth of films made of $Sn_2P_2S_6$ is reported from N.I. Dovgoshey [2] who used flash- and laser evaporation techniques. Rogach et al. [73] report the production of films by "thermal vacuum evaporation in a quasi-closed volume". They used powder of $Sn_2P_2S_6$ and different substrates such as p-type silicon (III), aluminium coated SiO_2 plates and pure aluminium as well. The crystallites had typical dimensions of 0.5 μm to 8 μm and the thickness of the film varied from 1 to 20 μm. Three different types of films can be grown: polycrystalline films, without preferred orientation, "textured films" with the ferroelectric axis in the plane of the film and "textured films" with the ferroelectric axis perpendicular to the substrate. The aim of this research is to produce ferroelectric "memory devices with non-destructive readout" [74]. Dielectric hysteresis loops gave a value of 1.0 $\mu C/cm^2$ for the spontaneous polarization and 0.6 $\mu C/cm^2$ for the remanent polarization. For switching pulses shorter than 2 μs and 10^9 pulses the poled state was still present. For industrial application the switching time is two orders of magnitude larger than what is typically employed in PZT or SBN. There is a huge market for such thin-film devices used in e.g. smart-cards. But the large dark conductivity in $Sn_2P_2S_6$ will impede the application since leakage currents are the major obstacle for integrated ferroelectric thin film devices.

Thermal treatment

For photorefractive oxides it is well known that thermal treatment drastically affects the fermi level and can therefore be employed for a fine-tuning of the charge-transfer-paths. The general concept is oxidation or reduction respectively i.e. annealing in reducing N_2 or sometimes H_2 [3] atmosphere or in oxidizing O_2 atmosphere. In $Sn_2P_2S_6$ the situation differs considerably from oxides since oxygen is not part of the lattice and will, if incorporated, possibly create oxides. Anyway oxygen will react as an extrinsic defect.

[2] Tonkie plyonki novykh slozhnyk poluprovodnikov, Uzghorod, UzhGU, 1985, only available in russian

[3] Hydrogen is likely to be built in and sometimes react as a migrating ion

Grabar [19] annealed nominally pure $Sn_2P_2S_6$ in sulfur atmosphere in quartz tubes and noticed a black cover that could be easily removed indicating either decomposition of the bulk crystal or production of a new chemical compound. No other significant change was observed. Detailed investigation of thermal treatment requires an advanced understanding of the material to anticipate the possible effects.

A.3 Stoichiometry

Although there is almost no literature available about the stoichiometry of $Sn_2P_2S_6$ it is likely that it plays a role in the charge transfer. For other materials such as $LiNbO_3$ or $LiTaO_3$, various features arise from non-stoichiometric samples. Direct measurement of the stoichiometry failed so far and indirect measurements by e.g. XPS are rather unreliable. The composition of the powder for the vapor transport is far from stoichiometry and as pointed out in [71] there is a considerable Sn overshoot. XPS measurements [75] reveal a significant tin overshoot and a sulfur deficiency within the experimental error:
$c_{Sn} : c_P : c_S = 22.487 \pm 1.236 : 21.297 \pm 2.288 : 56.363 \pm 1.643$

$(\mathbf{Pb}_{1-x}\mathbf{Sn}_x)_2\mathbf{P}_2(\mathbf{Se}_{1-y}\mathbf{S}_y)_6$

The composition given in the section heading is the most general one for the family of $Sn_2P_2S_6$-like crystals. The replacement of tin by lead and the replacement of sulfur by selenium as well as their combination lead to a wide spread in properties that have been subject of various investigation. Since the replacement of tin by lead and sulfur by selenium both decrease the phase transition temperature, the solid solutions with $x = 0$ or $y = 0$ are paraelectric at 295 K and lose all their potential for ferroelectric applications.
Nevertheless these complex phase diagrams depending on temperature, pressure and composition gave deep insight into the nature of the critical phenomena at the occurring phase transitions.

Incommensurate phase

An amazing property of $Sn_2P_2S_6$ is the existence of an incommensurate phase (ICP) of type II i.e. a modulation of ferroelectricity along a vector that is not parallel to the spontaneous polarization.

In $Sn_2P_2S_6$ this phase can be created in different ways:

Hydrostatic pressure exceeding 0.2 GPa creates this ICP

Selenium in replacement of sulfur creates the ICP for $c_{Se} > 29\%$.

Slow cooling and stabilization of the temperature slightly above T_C leads to the formation of the ICP [76].

This ICP has some peculiarities: the temperature range to observe the ICP can be widened under laser irradiation [65] and, if the temperature is slightly changed in the range of the ICP, there is no observable elongation. This phenomenon is known as 'invar-effect'. The widening of the ICP range by laser light works better if the electric field vector of the linearly polarized laser beam points along the spontaneous polarization vector so the electric field is large enough to cause a permanent displacement of the tin.

Appendix B

Electric field in ferroelectrics

We need to consider the correlation between the polarization and the internal electric field.

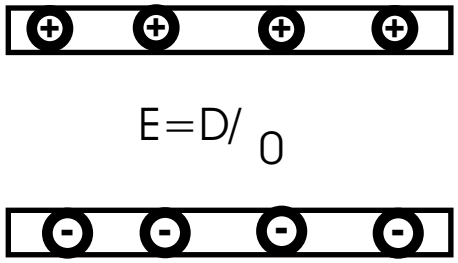

Figure B.1: *Most simple case: a capacitor in vacuum (relative permitivity $\epsilon = 1$).*

For simplicity let us consider a cubic material in a capacitor:

$$D = \epsilon\epsilon_0 E = \epsilon_0 E + P \tag{B.1}$$

$$P = E\epsilon_0(\epsilon - 1) \tag{B.2}$$

What is the mentioned field E? This is the macroscopic electric field inside the capacitor, usually defined by the charges on the electrodes of a capacitor:

$$E = \frac{Q}{\epsilon\epsilon_0 A} = \frac{\sigma}{\epsilon\epsilon_0} \tag{B.3}$$

So the field of the charges Q on the surface A is shielded by the relative permitivity ϵ. The fraction Q/A is usually denoted σ, the surface charge density. What is the underlying mechanism? Inside the dielectric material, we find dipoles (see Fig. B.2) that are either created or orientated by the field of the surface charge density.

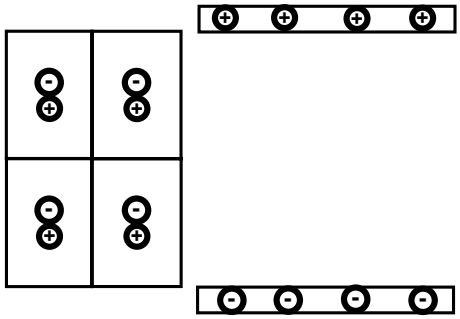

Figure B.2: *Inside a ferroelectric we have dipoles that are already orientated without external field.*

When the ferroelectric is inserted between the faces of a capacitor the dipole moments change: we have charges separated inside the material. According to the Gaussian law the effect can be expressed by surface charges alone. The field caused by these surface charges on the electrodes of an externally applied voltage have the opposite sign of the previously applied field. It is therefore often referred to as the depolarization field. In this way, inside the crystal the external electric field is decreased by a factor that expresses the ability of a material to produce a dipolemoment: ϵ.

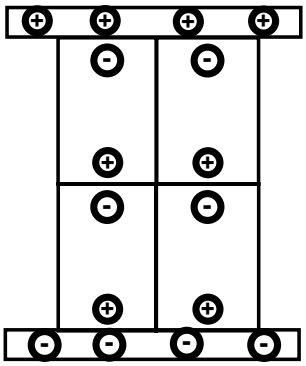

Figure B.3: *With external surface charges the internal dipoles elongate and partially compensate the external field by ϵ.*

The situation is totally different if we have no external voltage but only a ferroelectric in vacuum. We discuss the idealized case without compensation of surface charges by ambient gas. Now the surface charges are a consequence of the internal dipoles as derived by the gaussian law. Consequently the internal field is given by the surface charges:

$$E = -\frac{P}{\epsilon_0} \tag{B.4}$$

This is a general consequence for all electric fields occurring from integration over changing dipole moments.

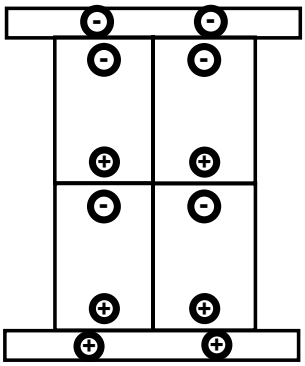

Figure B.4: *A volume of polarized matter is equivalent to a charged capacitor with $\sigma = P$ according to Eq. B.4.*

B.1 Internal fields

In ferroelectrics different external parameters can induce internal electric fields that feed back to other material properties as shown in Fig. B.5. In $Sn_2P_2S_6$ all of the external parameters given in this figure are reported to induce (partially lasting) internal electric fields. Thermal energy, as discussed in chapter 5, induces a pyroelectric field. Mechanical stress causes a piezoelectric field while the electric field of a laser beam affects the stability of the incommensurate phase. Externally applied electric fields are reported to cause 'photoelectret states' with lasting internal electric fields.

The observation of lasting internal fields after an applied voltage is removed

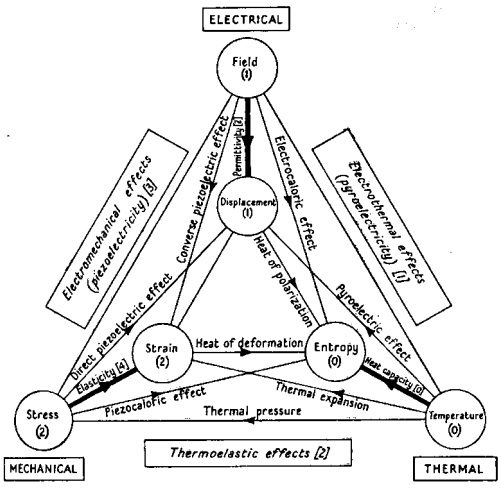

Figure B.5: *Dependence of crystal tensors depending on external parameters according [25].*

is peculiar. Apart from local dipole fields that are limited in range to the unit cell, all internal fields are sooner or later short-circuited by dark conductivity. In $Sn_2P_2S_6$ this results in a typical Maxwell time of a few seconds. Even the effect of local dipoles on the macroscopic crystal is short-circuited. A detailed investi-

gation of these local dipoles in $Sn_2P_2S_6$ is therefore worth doing to unravel the origin of these persistent fields.

Appendix C

Automatization

C.1 Evaluation of OMA data

We use Matlab© 5.3 (release 11.1) to evaluate our data. Since the typical size of a data matrix is less than 1024×34[1] there is no need for a high performance computer. The program *cycle.m* starts a sequence of Matlab functions to load a specific file created with *vtak.exe* that contains all necessary information. *cycle.m* distinguishes automatically between OMA II, OMA III and OMA IV files and allows to select a region with a satisfactory signal-to-noise-ratio. The data are smoothed over 40 points, but since the band width is much larger, this procedure does not affect physics.
The change of absorption is presented in a common line plot and a pseudo-3D plot. In addition to the former version of *cycle.m*, written by R. Scharfschwerdt, the present version allows the presentation in any of MATLAB's 3-D modes. Furthermore it is possible to obtain gradients of the maps, which is of interest for measurements with only small changes. Two dimensional cuts are available via mouseclick, so that photo-EPR evaluation is done much faster. Whenever it is necessary to investigate specific regions with comparably small absorption change, it is useful to select a value range. Often we compare pronounced deep temperature behavior with weak or negligible room temperature signals. This is immediately done with the *'symmetric' colorbar* option.
As an option to trace the correct measurement process, the time-stamps are presented in a diagram. Strong scattering of the values indicates problems during the measurement. If it is necessary to process the data, the images can be exported into different formats e.g. *.eps, *.ps, *.png, *.jpg.
For kinetic studies in $BaTiO_3$ and $Ba_{0.77}Ca_{0.23}TiO_3$ (C. Veber and M. Meyer) the kinetic mode data processing was established. The transmission data are transferred to absorption data, presented in a pseudo-3D plot over probe energy

[1] Our PDA has 1024 pixels. A measurement usually includes two runs with 17 excitation energies each. Since we usually cut off the noisy signals for $E_{probe} > E_{gap}$ we make use of less than 1024 pixels.

and time and stored automatically. All these functions are menu-controlled or realized by graphical user interfaces (GUI).

C.2 Determination of g-tensors

All g-tensor elements are determined with V. Grachev's program toolkit [77]. Some special approximating algorithms are used [78]. Depending on the low SNR it was sometimes inevitable to use other means to define the resonance position. Therefore a MATLAB script was written to have a complete angular dependence in one matrix and to automatically trace one resonance throughout a rotation. Even resonances that could hardly be figured out in the noise of a single spectrum were available in such a roadmap.

Bibliography

[1] R. Ryf, G. Montemezzani, P. Günter, A.A. Grabar, I.M. Stoyka, "Interband photorefraction at visible wavelength in $Sn_2P_2S_6$ crytals". *OSA TOPS* **27**, 80–85 (1999).

[2] S.G. Odoulov, A.N. Shumelyuk, U. Hellwig, R.R. Rupp, A.A. Grabar, I.M. Stoika, "Photorefraction in tin hypothiodiphosphate in the near infrared". *J. Opt. Soc. Am. B* **13 (10)**, 2352 (1996).

[3] A.A. Grabar, R.I. Muzhikash, A.D. Kostyuk, Yu.M. Vysochanskii, "Investigation of the switching process in the domain structure of ferroelectric $Sn_2P_2S_6$ by the dynamic holography method". *Sov. Phys. Solid State* **33 (8)**, 1314 (1991).

[4] A.A. Grabar, "Ferroelectric domains and photorefractive effect in $Sn_2P_2S_6$". *Ferroelectrics* **170**, 133 (1995).

[5] G. von Bally, F. Rickermann, S.G. Odoulov, A.N. Shumelyuk, "Near-infrared holographic recording in $Sn_2P_2S_6$ with nanosecond pulses". *Phys. stat. sol. (a)* **157**, 199 (1996).

[6] S. G. Odoulov, A.N. Shumelyuk, G.A. Brost, K.M. Magde, "Enhancement of beam coupling in the near infrared for tin hypothiodiphosphate". *Appl. Phys. Lett.* **69 (24)**, 3665 (1996).

[7] A.N. Shumelyuk, S.G.Odoulov, Hu Yi, E. Krätzig, G. Brost, "Ti:sapphire laser beam coupling in $Sn_2P_2S_6$". *conference contribution at CLEO'98,* 171 (1998).

[8] I. Seres, S. Stepanov, A.N. Shumelyuk, S. Odoulov, S. Mansurova, "Non-steady-state photo-EMF effect in fast $Sn_2P_2S_6$ photorefractive crystal". *J. Opt. Soc. Am. B* **17**, 1986–1991 (2000).

[9] A.A. Grabar, I.V. Kedyk, M.I. Gurzan, I.M. Stoyka, A.A. Molnar, Yu.M. Vysochanskii, "Enhanced photorefractive properties of modified $Sn_2P_2S_6$". *Opt. Comm.* **188**, 187–194 (2001).

[10] K. Buse, "Light–Induced Charge Transport Processes in Photorefractive Crystals I: Models and Experimental Methods". *Appl. Phys. B* **64**, 273 (1997).

[11] V. Caciuc, "private communication". (2001).

[12] G.M. Currò, V. Grasso, F. Neri, L. Silipigni, "An x-ray photoemission spectroscopy of the $Sn_2P_2S_6$ monoclinic II phase". *Il Nouvo Cimento* **20 D**, 1163 (1998).

[13] W. Klingen, G. Eulenberger, H. Hahn, "Über Hexachalkogenohypodiphosphate vom Typ $M_2P_2X_6$". *Naturwissenschaften* **57**, 88 (1970).

[14] C.D. Carpentier, R. Nitsche, "Vapour growth and crystal data of the thio(seleno)-hypodiphosphates $Sn_2P_2S_6$, $Sn_2P_2Se_6$, $Pb_2P_2S_6$, $Pb_2P_2Se_6$ and their mixed crystals". *Mat. Res. Bull.* **9**, 401–410 (1974).

[15] G. Dittmar, H. Schäfer, "Die Struktur des Di-Zinn-Hexathiohypodiphosphates $Sn_2P_2S_6$". *Z. Naturforsch.* **29 (b)**, 312 (1974).

[16] A.A. Grabar, A.I. Bercha, I.M. Stoika, "Three-dimensional probing of the domain structure in a uniaxial ferroelectric". *Tech. Phys. Lett.* **22 (1)**, 1 (1996).

[17] S.W.H. Eijt, R.Currat, J.E. Lorenzo, S. Katano, P. Saint-Gregoire, B. Hennion, Yu.M. Vysochanskii, "Soft modes and phonon interactions in $Sn_2P_2S_6$ and $Sn_2P_2Se_6$ studied by inelastic neutron scattering". *poster session II, ECAPD-3* (1996).

[18] T.K. Barsarmian, S.S. Khasanov, V.Sh. Shekhtman, "Diffraction analysis of incommensurate phases in crystals of quasi-binary $Sn_2P_2(S_{1-x}Se_x)_6$". *Ferroelectrics* **138**, 63 (1993).

[19] A.A. Grabar, "private communication". (2000).

[20] C.D. Carpentier, R. Nitsche, "Ferroelectricity in $Sn_2P_2S_6$". *Mat. Res. Bull.* **9**, 1097 (1974).

[21] B.Scott, M. Pressprich, R.D. Willet, D.A. Cleary, "High Temperature Crystal Structure and DSC of $Sn_2P_2S_6$". *J.Sol.State.Chem.* **96**, 294 (1992).

[22] A.P. Buturlakin, M.I. Gurzan, V.Yu. Slivka, "Ferroelectric properties of $Sn_2P_2S_6$ crystals". *Sov. Phys. Solid State* **19 (7)**, 1165 (1977).

[23] S.L. Bravina, L.S. Kremenchugskii, M.D. Kladkevich, N.V. Morozovskii, V.B. Samoilov, M.M. Maior, M.I. Gurzan, Yu.M. Vysochanskii, V.Yu. Slivka, "Pyroelectric properties of $Sn_2P_2S_6$ crystals". *Izvestiya Akademii Nauk SSSR, Neorganicheskie Materialy* **23(5)**, 733–738 (1987).

[24] M.M. Maior, Yu. M. Vysochanskii, I.P. Prits, Sh. B. Molnar, L.A. Seikovskaya, V. Yu. Slivka, "Pyroelectric properties of oblique cuts of an $Sn_2P_2S_6$ crystal". *Sov. Phys. Crystallogr.* **35(5)**, 767–769 (1990).

[25] J.F. Nye, *Physical properties of crystals: their representation by tensors and matrices*. Oxford Clarendon Press, 1985.

[26] U. Hellwig, "Thesis: Untersuchungen des photorefraktiven Effektes in $Sn_2P_2S_6$". 53 (1998).

[27] A.A. Grabar, "Light-induced electric conductivity in $Sn_2P_2S_6$". *Ferroelectrics* **192**, 155 (1997).

[28] A.V. Gomonnai, B.M. Koperles, I.I. Groshik, M.I. Gurzan, "Thermal expansion of $Sn_2P_2S_6$ and SbSI crystals near ferroelectric phase transition". *Sov. Phys. Solid State* **22 (3)**, 546 (1980).

[29] S.G. Odoulov, "private communication". (2000).

[30] I.V. Kityk, V.Yu. Fenchak, A.A. Grabar, V.Yu. Slivka, "Band structure and optical spectra of the ferroelectric semiconductor $Sn_2P_2S_6$". *Phys. Solid State* **37 (6)**, 1025 (1995).

[31] R. Becker, W. Brockner, "Kristallstruktur und Schwingungsspektren des Di-Blei-Hexathiohypodiphosphates $Pb_2P_2S_6$". *Z. Naturforsch.* **38a**, 874–879 (1983).

[32] M. P. Petrov, I. A. Sokolov, S. I. Stepanov, G. S. Trofimov, "Non–Steady–State Photo–Electromotive–Force Induced by Dynamic Gratings in Partially Compensated Photoconductors". *J. Appl. Phys.* **68**, 2216 (1990).

[33] Yu.M.Vysochanskii, M.M. Maior, V.A. Medvedev, V.M. Rizak, V.Yu. Slivka, E.A. Sorkin, "Low-temperature specific heat and pyroactivity of ferroelectric crystals of the system $Sn(Pb)_2P_2S(Se)_6$". *Sov. Phys. Crystallogr.* **35(4)**, 541–544 (1990).

[34] U. Hellwig, "Thesis: Untersuchungen des photorefraktiven Effektes in $Sn_2P_2S_6$". (1998).

[35] H. Kröse, R.Scharfschwerdt, A. Mazur, O.F.Schirmer, "A multichannel spectrometer for correlated EPR-optical absorption analysis of photochromic processes in crystals". *Appl. Phys. B* **67**, 79–86 (1998).

[36] Heinz-Helmut Perkampus, *UV-VIS spectroscopy and its applications.* Springer (Berlin u.a.), 1992.

[37] Osram GmbH, "private communication". (1999).

[38] J.A. Weil, J.R. Bolton, J.E. Wertz, *Electron Paramagnetic Resonance.* Wiley Interscience Publication, 1994.

[39] G.E. Pake, T.L. Estle, *The physical principles of electron paramagnetic resonance.* W.A. Bejamin, Inc., 1973.

[40] S.L. Bravina, N.V. Morozovsky, A.K. Kadashchuk, V.S. Manzhara, "Low-temperature pyroelectric and luminescence phenomena in $Sn_2P_2S_6$ single crystals". *Ferroelectrics* **192**, 197 (1997).

[41] Y. Ohmori, M. Yamaguchi, K. Yoshino, Y. Inuishi, "Electron Hall Mobility in Reduced $LiNbO_3$". *Jpn. J. Appl. Phys.* **15**, 2263 (1976).

[42] M. Wierschem, "private communication". (2000).

[43] M. Iwata, A. Miyashita, Y. Ishibashi, K. Moriya, S. Yamo, "Low temperature dielectric dispersion in $Sn_2P_2S_6$". *Journal of the Physical Society of Japan* **67**, 499–501 (1998).

[44] A.N. Shumelyuk, "private communication". (2001).

[45] T. Castner et al., . *J. Chem. Phys.* **32**, 668 (1960).

[46] O.F. Schirmer, E.K.H. Salje, . *J.Phys.C: Solid St. Phys* **13**, L1067 (1980).

[47] G. Schmidt, J. Petersson, "Über die Lichtemission von ferroelektrischen Triglyzinsulfatkristallen". *Z. Naturforsch.* **24a**, 1559–1562 (1969).

[48] H.P. Yockey, C.L. Aseltine, "Development of high voltages in potassium dihydrogen phosphate irradiated by γ rays". *Physical Review B* **11**, 4373 (1975).

[49] D.W. Cooke, Jr. C. Alexander, "Observations of intense scintillations in unirradiated glycine". *Physical Review B* **14**, 1333 (1976).

[50] K.S.V. Nambi, "Pyroluminescence induced by tourmaline". *Phys. stat. sol. (a)* **82**, K71–K73 (1984).

[51] K.A. Mirza, P.D. Townsend, G.L. Destefanis, "Light emission from the surface of $LiNbO_3$". *Phys. Stat. Sol. (a)* **47**, K63 (1978).

[52] I. Tale, V. Tale, J. Rosa, "The field fluctuational model of thermally stimulated processes in ferroelectric $LiNbO_3$". *Solid State Communication* **48**, 135 (1983).

[53] S.L. Bravina, A.K. Kadashchuk, N.V. Morozovskii, N.I. Ostapenko, Yu.A. Skryshevskii, M.T. Shpak, "Pyroluminescence of proustite an pyrargyrite crystals". *Sov. Phys. Tech. Phys.* **33 (7)**, 834 (1988).

[54] J.S. Patel, D.M. Hanson, "Pyroelectric luminescence from ionic compounds". *Ferroelectrics* **38**, 923 (1981).

[55] Z. Dreger J. Kalinowski, R. Nowak, J. Sworakowski, "Pyroelectric luminescence of N-isopropylcarbazole single crystals". *Chemical Physics Letters* **116**, 192–196 (1985).

[56] J.S. Patel, D.M. Hanson, "Pyroelectric luminescence". *Nature* **293**, 445 (1981).

[57] J. Kalinowski, Z. Dreger, "Simple model for pyroelectric luminescence". *Physical Review B* **36**, 7840–7848 (1987).

[58] C. Kittel, *Introduction to solid-state physics.* Wiley, 1986.

[59] S.B. Lang, *Sourcebook of pyroelectricity.* Gordon Breach, 1974.

[60] J. Frenkel, "On Pre-Breakdown Phenomena in Insulators and Electronic Semi-Conductors". *Phys. Rev.* **54**, 647/648 (1938).

[61] J.M. Meek, J.D. Craggs, *Electric Breakdown of Gases.* Wiley, 1978.

[62] J. Kalinowski, J. Godlewski, Z. Dreger, P. Mondalski, "Pressure-induced luminescence of N-isopropylcarbazole single crystals". *Chemical Physics Letters* **128**, 480–482 (1986).

[63] Yu.I. Tyagur, J. Jun, "The influence of high hydrostatic pressure on phase transitions temperature in ferroelectric crystals of $(Pb_ySn_{1-y})_2P_2(Se_xS_{1-x})_6$ family". *Ferroelectrics* **192**, 187–195 (1997).

[64] Yu.I. Tyagur, E.I. Gerzanich, "The p-T phase diagram of the ferroelectric $Sn_2P_2S_6$". *Sov. Phys. Cristallogr.* **29(5)**, 563 (1984).

[65] Yu.M. Vysochanskii, V.G. Furtsev, M.M. Khoma, M.I. Gurzan, V. Yu. Slivka, "Splitting of the ferroelectric phase transition in a laser radiation field and self-focussing of light in the incommensurate phase". *Sov. Phys. JETP* **62(3)**, 540 (1985).

[66] Yu.M. Vysochanskii, E.I. Gerzanich, A.A. Grabar, M.M. Maior, S.I. Perechinskii, L.A. Salo, A.G. Slivka, V.Yu. Slivka, Yu.I. Tyagur, M.M. Khoma, "Phase diagrams of mixed crystals of the $Sn_2P_2S_6$ type: phenomenological analysis and lattice dynamics". *Sov. Phys. Cristallogr.* **30(6)**, 650 (1985).

[67] E. Glatzel, . *Z. anorg. Chemie* **4**, 186 ff (1893).

[68] M. C. Friedel, C.R. Hebd, "Bull. Soc. Chim. France". **11**, 115 ff (1894).

[69] L. Ferrand, . *Bull. Soc. Chim. France* **13**, 115 ff (1895).

[70] K. Küpper, "Photoelektronenspektroskopie an photorefraktiven Materialen". *Master thesis at the department of physics in Osnabrueck,* **chapter 4**, 48 (2001, unpublished).

[71] X. Bourdon, E. Prouzet, V.B. Cajipe, "Room-temperature synthesis of $Sn_2P_2S_6$". *J.Sol.State.Chem.* **129**, 157 (1997).

[72] I.V. Kityk, R.I. Mervinskii, J. Kasperczyk, S. Jossi, "Synthesis and properties of nm-sized $Sn_2P_2Se_6$ single crystals embedded in photopolymeric host". *Mat.Lett.* **27**, 233 (1996).

[73] Ye.D. Rogach, E.A. Sachvenko, D.N. Sanjiev, N.P. Protsenko, A.I. Rodin, "Film structures based on the ferroelectric-semiconductor $Sn_2P_2S_6$". *Ferroelectrics* **83**, 179–185 (1988).

[74] E. Arnautova, E. Sviridov, E. Rogach, E. Savchenko, A. Grekov, "$Sn_2P_2S_6$ films for memory devices with nondestructive readout". *Intergrated ferroelectrics* **1**, 147 (1992).

[75] U. Hellwig, "Thesis: Untersuchungen des photorefraktiven Effektes in $Sn_2P_2S_6$". 39 (1998).

[76] A.A. Molnar, Yu.M. Vysochanskii, A.A. Horvat, Yu.S. Nakonechnii, "Critical phenomena in ferroelectric-semiconductor crystals $Sn_2P_2S_6$: dielectric investigation". *Ferroelectrics* **192**, 137 (1997).

[77] V. Grachev, "Visual EPR". *http://www.physik.uni-osnabrueck.de /resonanz/Grachev/* (release 2001).

[78] V.G. Grachev, Yu.G. Semenov, "Methods of computer treatment of EPR and ENDOR spectra". *Radiospectrocopy* 163–171 (1983).

Acknowledgments

Most of all I would like to thank Prof. O.F. Schirmer for the supervision of this thesis, his readiness for discussion and his patient support to get familiar with EPR.
Thanks to all members of the team "Magnetische Resonanzspektroskopie", especially to my 'roommate' Christophe Veber, since his skills in VC++ made the OMA II/3/4 run and to Martin Meyer for his assistance with optical absorption measurements.
It was a pleasure to cooperate with Prof. S.G. Odoulov, his coworker Dr. Sasha Shumelyuk and our partners in the DFG project 436 UKR 18/4/00, Dr. Andrey Kadashchuk and his coworker Dr. Y. Skryshevsky from the Institute of Physics, National Academy of Sciences, Kiev, Ukraine. Especially Sasha's experience with holography provided important help to see the charge transfer subtleties in $Sn_2P_2S_6$.
Andrey and Yury performed the luminescence measurements. I am grateful for all kind of support and for the great time we all had in Kiev.
A.A. Grabar helped me a lot with various unpublished details on the growth and thermal treatment of $Sn_2P_2S_6$.
The band structure calculations from Dr. A. Postnikov were a valuable contribution to the explanation of the electron center in $Sn_2P_2S_6$.
Big thanks to W. Schniederberend and H. Heine representing their teams who always managed to find an appropriate solution for any technical problem.
Financial support of the Deutsche Forschungsgemeinschaft (DFG) within the projects 146 UKR 18/4/00 and 17/11/00 is gratefully acknowledged.

Erklärung nach §3 der Promotionsordnung
Hiermit erkläre ich an Eides Statt, daß ich die vorliegende Arbeit selbständig und ohne unerlaubte Hilfe verfaßt und die verwendeten Hilfsmittel vollständig angegeben habe.

Osnabrück, den

Andreas Rüdiger